Feasibility Study of Spatial-Phase-Locked Focused-Ion-Beam Lithography

by

Anto Yasaka

M.Eng., Nuclear Engineering, Tokyo Institute of Technology, 1983
B.S., Applied Physics, Tokyo Institute of Technology, 1981

Submitted to the Department of Materials Science and Engineering
in partial fulfillment of the requirements for the degree of

Master of Science
in Materials Science and Engineering

at the

MASSACHUSETTS INSTITUTE OF TECHNOLOGY

June, 1995

Signature of Author .....
Department of Materials Science and Engineering
May 12, 1995

Certified by.....
Henry I. Smith
Professor of Electrical Engineering
Thesis Advisor

Certified by.....
Carl V. Thompson II
Professor of Electronic Materials
Thesis Advisor

Accepted by.....
Carl V. Thompson II
Professor of Electronic Materials
Chair, Departmental Committee on Graduate Students

Feasibility Study of Spatial-Phase-Locked Focused-Ion-Beam Lithography

by

Anto Yasaka

Submitted to the Department of Materials Science and Engineering
in partial fulfillment of the requirements for the degree of

Master of Science
in Materials Science and Engineering

Abstract

It is known that focused-ion-beam lithography has the capability of writing extremely fine lines (less than 50 nm line and space has been achieved) without proximity effect. However, because the writing field in ion-beam lithography is quite small, large-area patterns must be created by stitching together the small fields. The precision with which this can be done is much poorer than the resolution, typical stitching errors are ~100 nm. A spatial-phase-locking method has been proposed to reduce stitching errors and provide both pattern placement accuracy and precision. The fundamental flaw in conventional particle-beam (electron and ion) lithography, which gives rise to most of the stitching error, is that the beam location is not directly monitored. The stage position is monitored via laser interferometer, but the beam location is not. Thus, the beam can drift from its assumed position due to thermal expansion, charging, or any other error sources. The spatial-phase-locking enables direct monitoring of beam location and closed loop beam positioning.

Spatial-phase-locking will be done by providing a global fiducial grid on the substrate itself, that is transparent to the exposing beam but which enables a control computer to keep track continuously of the beam location and correct any drift. The grid consisting of a polymer grid pattern on a thin metal film (e.g., 20 nm thick Al) will be created by interferometric lithography, which ensures long-range spatial-phase coherence. As the beam is scanned across the grid pattern the secondary-electron emission is strongly modulated since the secondary yields of Al and polymer differ significantly. This periodic signal is used by the control computer as a beam-position signal against which the pattern writing can be locked.

In this study, ion induced electron emission yields from various materials such as Al, Si, and PMMA has been investigated to evaluate the feasibility of spatial-phase-locked focused-ion-beam lithography and to optimize the substrate configuration for ion beams.

Thesis advisor: Henry I, Smith
Title: Professor of Electrical Engineering

Thesis Advisor: Carl V. Thompson II
Title: Professor of Electronic Materials

Acknowledgment

I would like to take this opportunity to thank those who have given me the support to carry out this research. First of all, I am indebted to my advisor, Prof. Henry I. Smith, for his invaluable advice and support. I would like to thank my co-advisor, Prof. Carl V. Thompson, for helpful suggestions. I am particularly grateful to Mr. Scott Silverman for helpful suggestions in carrying out this research and for reading the entire manuscript and making a number of critical comments. I am thankful to Mr. Sergey Etchin for his kind assistance in the FIB operation. I am also grateful to Mr. Mark Mondol for providing me with the samples. All members of the NSL staff and students deserve many thanks: Jim Carter, Vincent Wong, Juan Ferrera, Martin Burkhardt, Nitin Gupta, Euclid Moon, Satyen Shah, Tim Savas, Tom Murphy, for their kindness and encouragement. Special thanks go to my employer, Seiko Instruments Inc., for giving me this exciting opportunity to study at MIT. I will always be grateful to my family for all their love and support. I hope to be able to repay them someday.

Contents

List of Figures

List of Tables

1. Introduction

In the last decade, line width dimension of microelectronic devices has been dramatically reduced while circuit complexity has increased. Consequently, the requirement for microfabrication technology reaches into the submicron and nanometer regime. In order to meet the requirements, the need has arisen for pattern generation and lithography systems with superior performance specifications.

Patterns are formed by exposing a wafer coated with a thin film of resist material that is sensitive to a corresponding pattern of the appropriate radiation and developing the resultant latent image. Depending on the radiation source and the type of resist, we characterize these techniques as optical, X-ray, electron beam, or ion beam lithography. These lithographies are utilized for mask making, image transfer, and direct writing. As the need for sub-100 nanometer resolution grows, the importance of particle beam (electron and ion) lithography increases, because of their capability of writing very fine patterns onto resist layer.

In this chapter, conventional optical lithography techniques are reviewed. Then, the basics of electron and ion beam lithography will be discussed with a focus on the pattern placement accuracy. A method called spatial phase locking used to enhance pattern integrity in electron beam lithography will be introduced. Then, focused ion beam technology and the interaction between ion beam and matter will be discussed. Finally, the objective of this study will be presented.

1.1 Optical Lithography

Optical lithography which utilizes a mercury vapor lamp as an illumination source has been a dominant technology for pattern transfer onto a silicon wafer in mass-production of integrated circuits (IC). The basic steps of conventional optical lithography techniques are shown in Fig. 1.1 [1]. First, a thin film of photoresist is spin-coated on the surface of the substrate to be patterned. A mask is interposed between a source of ultraviolet radiation and the resist-coated film. The mask contains the pattern information to be transferred to the resist layer in a manner that depends on the type of resist (positive or negative, as

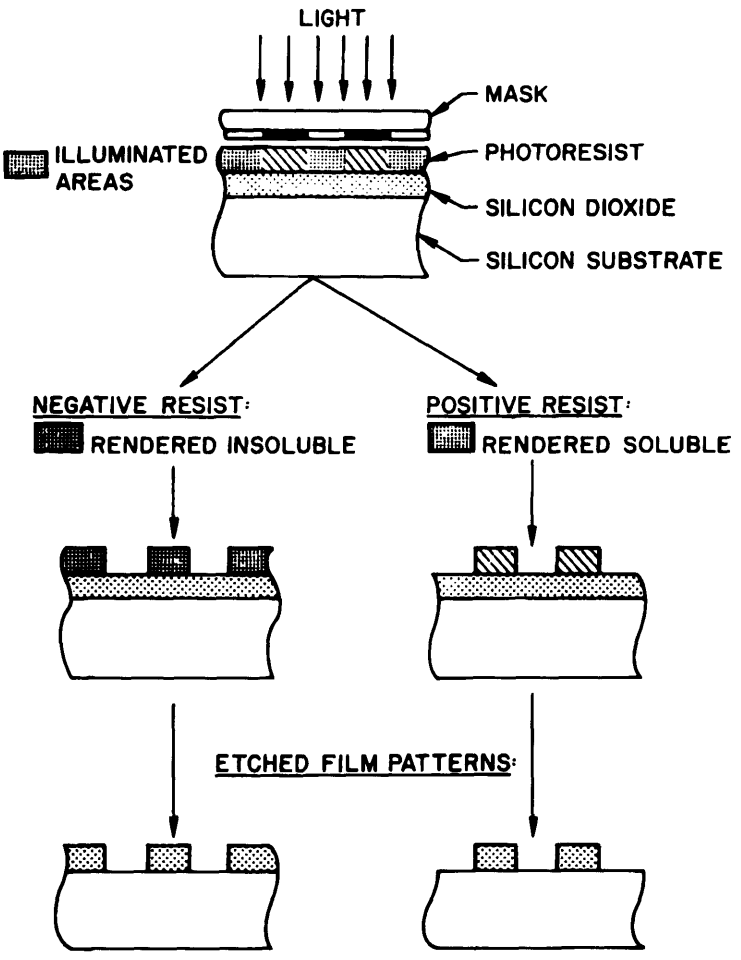

Fig. 1.1: Schematic of exposure and development processes using positive and negative resists [1].

shown in Fig 1.1). The patterns in the resist are formed by removing a part of the resist layer through the development process. Areas where resist is removed are then subjected to an additive or subtractive process. Oxidation, ion implantation, diffusion, and metallization are examples of additive processes while wet and dry etching are typical subtractive processes. Areas where resist remains act as a protective mask of the underlying film during the subsequent processes. The number of masks used in the typical IC fabrication process is 10 to 20 so that the steps described above are repeated many times to complete the process.

In addition to the contact printing depicted in Fig. 1.1, one can also employ projection lenses. The resolution of optical projection lithography can be described using the Raleigh criterion for resolution, expressed in the following form:

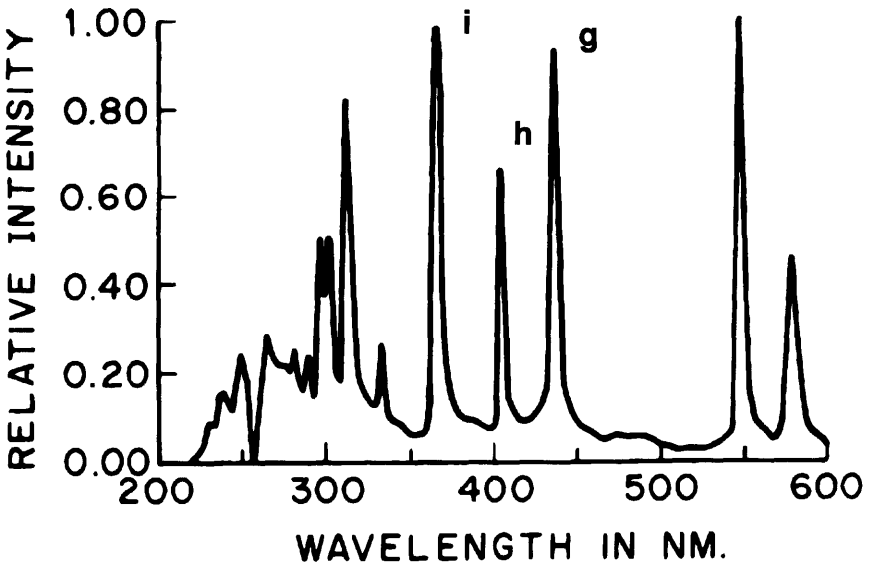

Fig. 1.2: High pressure mercury-arc spectrum [1].

$$d = k\frac{\lambda}{NA}, \tag{1.1}$$

where d is the smallest resolvable feature, k is a constant, λ is the wavelength of the radiation, and NA is the numerical aperture, defined as

$$NA = n \sin \alpha, \tag{1.2}$$

where n is the refractive index and 2α is the acceptance angle of the objective lens. The constant k depends on the type of photoresist and also on the method of exposure. Typical values for k range from 0.5 to 1.0. This criterion predicts that the use of a shorter wavelength radiation source and higher NA lens will result in better resolution. However, the depth of focus, DOF, is inversely proportional to the square of the NA,

$$DOF = k'\frac{\lambda}{(NA)^2}, \tag{1.3}$$

where k' is another constant. So as the wavelength is reduced or the NA is increased to produce smaller features, it becomes more difficult to maintain focus on a wafer with relatively severe topography. It is more desirable to decrease the wavelength to attain the small image size than to increase NA due to the strong dependence of the depth of focus on the latter. Fig. 1.2 shows a spectral distribution for a high pressure mercury arc source. The typical optical lithography system for the production of very large scale integrated circuits (VLSI) utilizes i-line (365 nm) as a radiation source and a lens of $NA = 0.4$ [2].

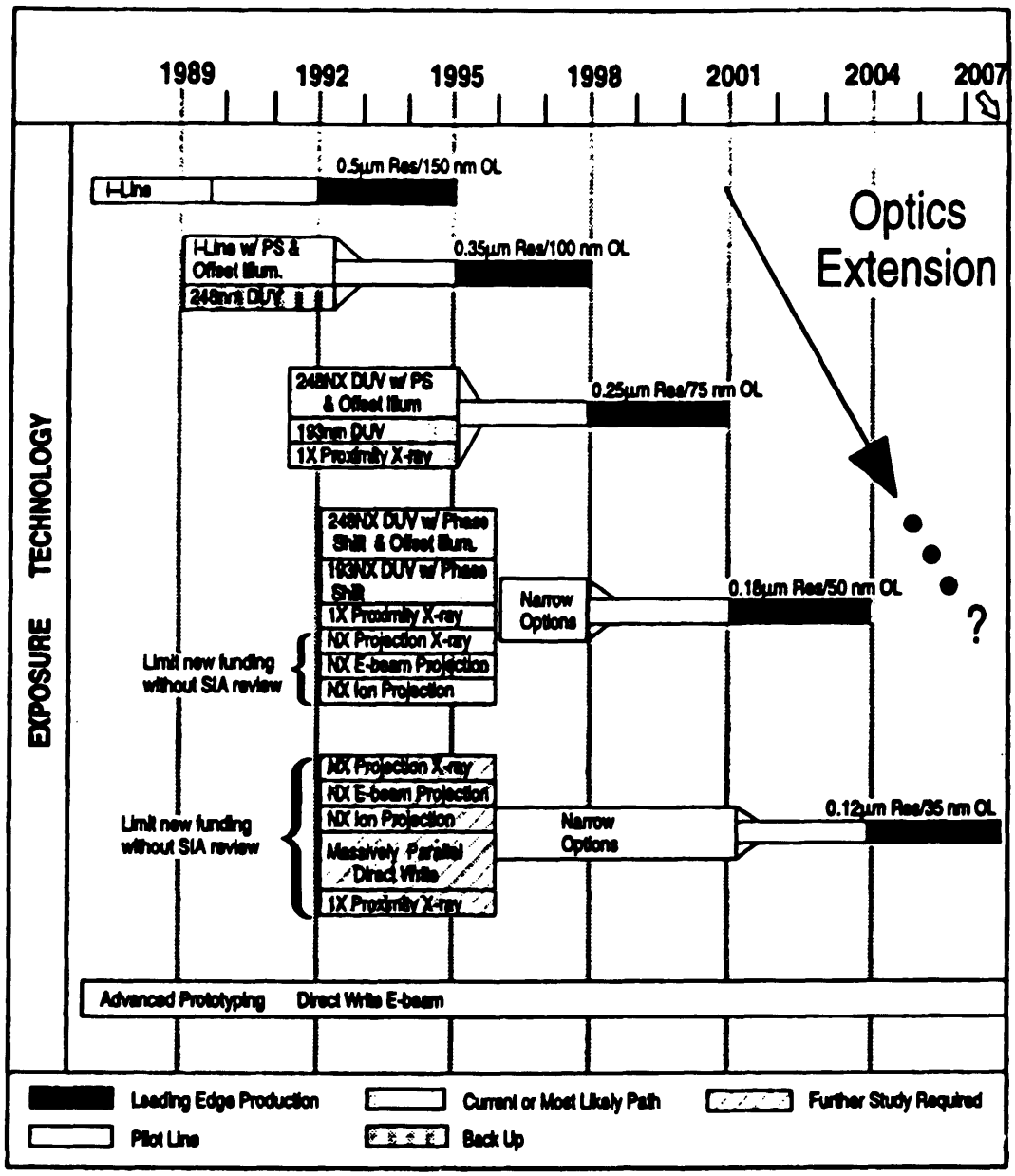

Fig. 1.3: Exposure technology roadmap by Semiconductor Industry Association [3].

The Raleigh criterion predicts that the resolution limit of the system is about 0.5 μm, assuming $k = 0.6$. This value does not meet the specification of the next generation VLSI, of which design rule is 0.35 μm. Therefore, interest in deep UV and X-ray lithography has been stimulated.

Fig. 1.3 illustrates the future trend of lithographic technology proposed by the Semiconductor Industry Association (SIA) in 1992 [3]. This road map indicates that

advanced technologies such as X-ray, electron beam, and ion beam will be the supersede for optical lithography in the sub-quarter micron era.

1.2 Electron Beam Lithography

When energetic particle beams (electron and ion) are used as a radiation source, there are two ways to irradiate resist surface and create a pattern. One is the parallel exposure of all or part of a pattern, the other is the sequential exposure of one pattern element at a time by scanning a beam. Projection systems generally have a high throughput and are less complex than scanning systems. The pattern information is stored in masks. The scanning systems are under computer control where a finely focused beam is used to generate the pattern, correct the distortion and proximity effect (when electron beam is used) and register the wafer position. The pattern information is stored in a digital memory.

Scanning electron beam lithography (SEBL) has gained in popularity as a tool for mask making, since direct control by a computer offers the ability to generate the patterns without the need for a mask. Fig. 1.4 shows the schematic of an SEBL system [1]. The SEBL system is in essence a scanning electron microscope (SEM), modified to perform lithography. Electrons are extracted from an electron source and accelerated to the sample by a potential difference. A set of lenses, which consist of magnetic or electric fields, focuses the electron beam to a small spot on the substrate. The beam can be deflected by means of two orthogonal electric or magnetic deflection fields, which are applied transversely to the trajectory of the beam. A beam blanker that consists of a pair of electrostatic electrodes works to turn the beam on and off by deflecting the beam off axis onto a beam stop. By integrating all these elements in an electron optical column, arbitrary patterns can be created on the substrate surface. The sample is coated with an e-beam resist, such as PMMA (poly methyl methacrylate), which is sensitive to electron irradiation. The beam under computer control is scanned over areas of any shape according to the stored pattern data. Thus the desired image can be selectively irradiated on the resist layer.

Since it is impossible to deflect the high energy electron beam (typically 10 - 50 keV) more than a few millimeters and keep it focused on the sample plane, the sample is set on a mechanical stage and moved through the deflection field of the beam in order to cover the entire area to be exposed. Large area patterns are created by means of stitching together small fields. To this end, stage position is monitored via a laser interferometer with nanometer resolution. Any error in the stage position is detected and a correction is fed to

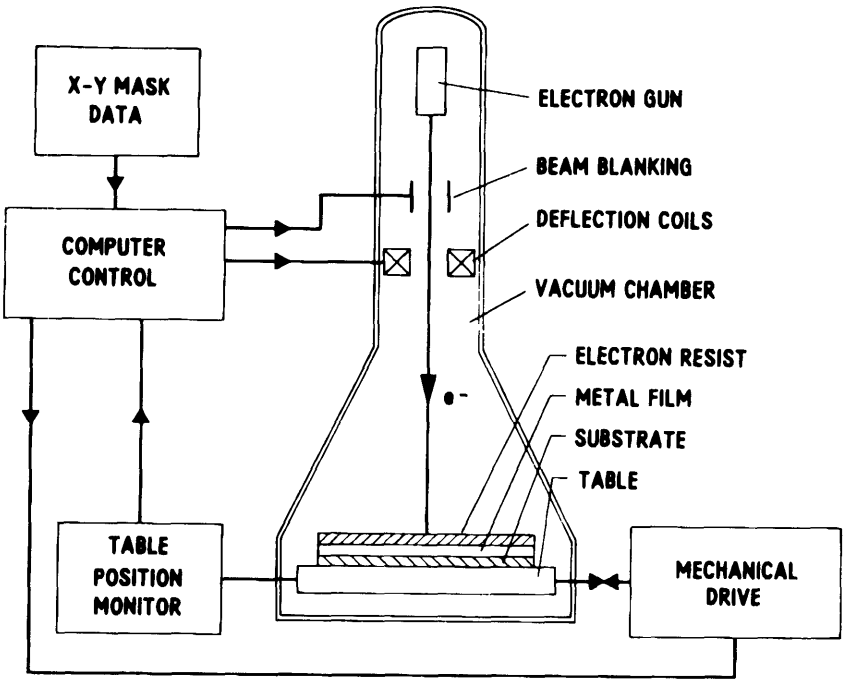

Fig. 1.4: Schematic of an electron beam lithography system [1].

the beam deflection electronics which shifts the scanning field to compensate for stage position error. In principle it should be possible to place features with this accuracy, but in practice several factors restrict the pattern placement accuracy of an SEBL system. Deviation from the ideal position at the boundaries between the small fields is called "stitching error". This will be discussed in detail later.

When an electron beam enters a material, it loses energy by interacting with resident atoms. The interaction between electrons and atoms is divided into two categories according to the collision process elastic and inelastic collisions. Elastic collision results only in a change of direction of the electrons while inelastic collision results in energy loss. Energy may be lost through creation of secondary electrons, inner shell ionizations that lead to x-ray and Auger electron emission, excitation of density oscillations in electron gas plasmas, creation of electron-hole pairs followed by photon emission (cathodoluminescence), and lattice vibration (phonon excitation). The incident electron beam undergoes multiple scatterings which lead to a broadening of the beam. Most of the electrons are forward scattered through small angles ($< 90°$) from their original direction. Some of the electrons experience large angle backscattering which causes them to return toward the surface. These broadened and scattered electrons cause exposure of the resist at points that can be quite remote from the initial entry point and result in developed resist

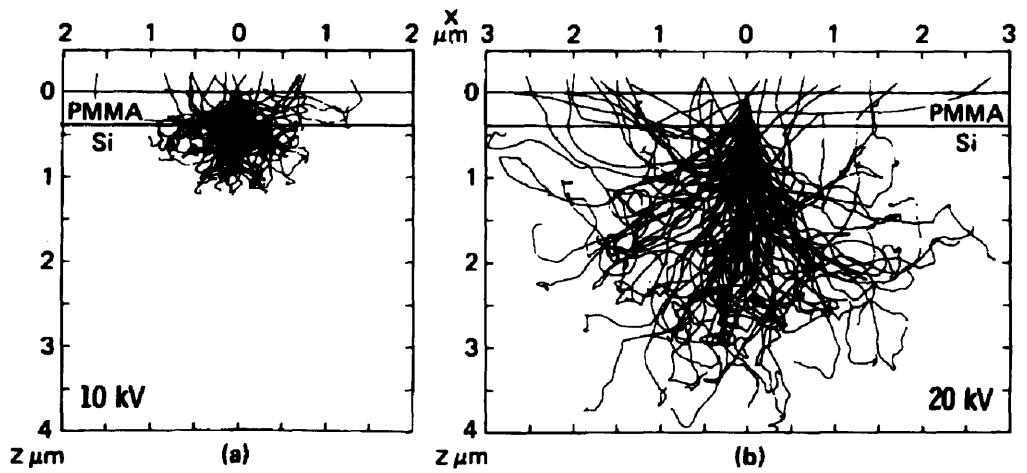

Fig. 1.5: Monte Carlo simulation of trajectories of 100 electrons scattered in a 0.4μm PMMA film coated on a silicon substrate [4].

images wider than anticipated from the beam diameter alone. Since the scattering can extend over several micrometers, depending on the electron beam energy (see Fig. 1.5), closely spaced patterns will receive electrons from the exposure of their neighbors. This resultant, undesired exposure of resist is known as the "proximity effect".

There are several ways to evaluate the influence of the electron scattering. One of the most useful approaches is the Monte Carlo method which simulates the trajectory of the electrons in the resist and substrate system. An example of the calculation result is shown in Fig. 1.5 [4].

The probability that an electron is scattered into a given angle θ, i.e., the differential scattering cross section, can be calculated using the Born approximation to the Schroedinger equation, with the Thomas-Fermi potential [5]. The result is given by [1]

$$\frac{d\sigma}{d\Omega} = \frac{Z(Z+1)e^4}{4m^2v^4[\sin^2(\theta/2)+\alpha^2]^2}, \tag{1.4}$$

where m is the mass of the electron, v is the velocity of the electron, Z is the atomic number of the target atom, and α is the atomic screening parameter expressed by

$$\alpha = 2.33Z^{\frac{1}{3}}E^{-\frac{1}{2}}, \tag{1.5}$$

where E is the energy of the electron. This implies that large angle electron tends to occur in material that consists of high Z atoms. Therefore, the proximity effect due to the backscattering from the substrate can be a serious problem for high Z x-ray masks such as low stress tungsten fabricated by SEBL.

Several countermeasures to compensate the proximity effect have been proposed [1][6]. One method that is adopted in most of the SEBL system is adjusting the electron irradiation pattern to correct for proximity effect. This is done by varying dosage and shape of each feature. In some cases, features are partitioned and each part is assigned a dose based on a proximity model. However, a throughput penalty may be incurred as a result, since increased computer time will be necessary to partition and expose the subdivided feature. Another countermeasure is the use of multi-layer resist techniques, with which the imaging resist layer is separated from the substrate by a thick, planarizing organic material. The planarizing layer absorbs backscattering electrons from the substrate, minimizing their effect on neighboring resist. Multi-layer resist systems, however, add processing complexity and create problems with registration mark recognition. The use of very high beam energy, ~100 keV, is another approach to lessen the severity of the proximity effect. What this does is to increase the range of the backscattered electrons. The backscattering is still present and of about the same magnitude, but it is spread out over a large area and hence the average background is lower.

It has been known that the use of ion beams instead of electron beams for resist exposure eliminates the proximity effect. In the early 80's, focused ion beam (FIB) technology attracted attention and has been applied in various practical fields, including maskless ion implantation, photomask defect repair, microcircuit modification and ion beam lithography. Several reports have shown the possibility of the focused ion beam lithography to fabricate very fine features on resist film [7][8][9][10]. In the next section, focused ion beam technology will be discussed.

1.3 Focused Ion Beam Technology

As discussed in previous sections, FIB lithography has high potential to play an important role in nanometer technology because of the lack of backscattered electrons. This may be especially important in fields in which backscattering electrons are a severe problem such as in patterning high-Z x-ray masks. Unlike electron beam technology, FIB technology (and FIB lithography in particular) is relatively new and there is still a need to accumulate basic knowledge through comprehensive and energetic research works. In this section, basic of FIB technology will be reviewed.

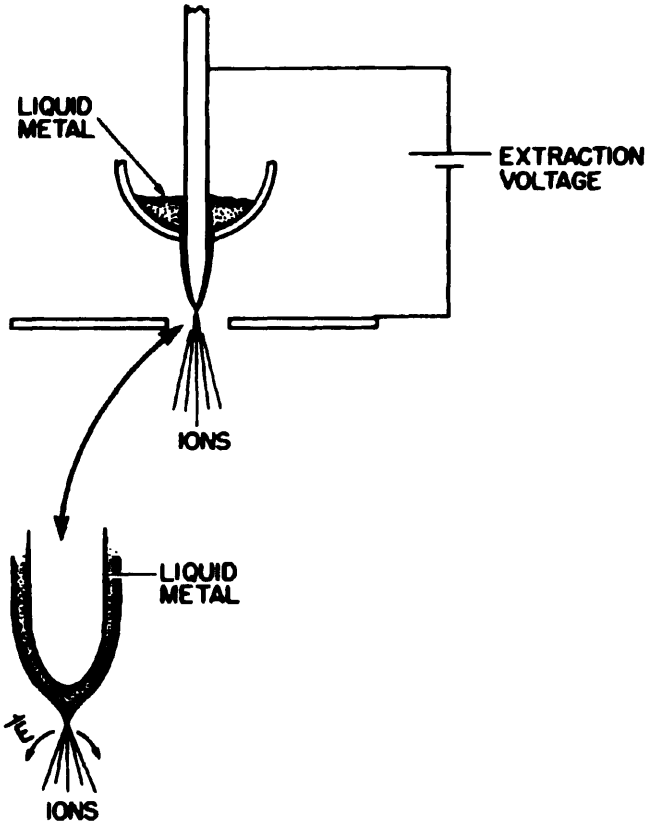

Fig. 1.6: Schematic of liquid metal ion source with enlarged view of tip showing liquid pulled into a cusp by the electric field [10].

1.3.1 Liquid Metal Ion Sources

The development of liquid metal ion sources (LMIS) has brought practical application of focused ion beam (FIB) technology to the semiconductor industry [11-16]. The high brightness of the LMIS has made it possible to focus ion beams with a current density of the order of 1 A cm^{-2} down to sub-micron diameters.

An LMIS usually consists of a needle emitter with an end radius of 1 - 10 μm, which is coated with a metal having a high surface tension and a low vapor pressure at its melting point. The emitter is heated to the melting point of the metal while a high positive voltage is placed on it relative to an extraction electrode. The liquid metal is drawn into a conical shape by the balance between the electrostatic and surface tension forces. The apex of the liquid cone is drawn to an end radius so small that the high electric field causes ions to begin to form through field evaporation. The cone apex is believed to have a radius of about 5 nm [17] [18]. The schematic is illustrated in Fig. 1.6. The most commonly used

source metal is Ga. Au/Si and Au/Si/Be alloys have also been used for lithography because these sources can supply lighter mass ions.

The two fundamental performance limitations are the virtual source size and the energy spread of the ions emitted from the source. Since the end radius of an operating LMIS is of the order of 5 nm in diameter, a total extracted current of only a few microamperes results in a very high source current density, ~10^6 A cm^{-2}. Consequently there are very significant space charge effects in the ion beam which have an important effect on the focusing properties of ion optical systems. The virtual source size (i.e., its effective ion optical diameter), therefore, is much larger than the physical diameter of the ion emitting region due to perturbations in the ion trajectories caused by Coulomb interactions near the source (typically 50 - 100 nm [19] [20]). This requires that demagnifying optical system be used to achieve smaller focal spots on the sample. The energy spread of the ions emitted from LMIS (5 - 20 eV) is much broader than the expected value for field evaporated ions, a fairly narrow 1 eV FWHM [21]. This is also caused by high current density at the emission point [22]. In fact, the energy distribution depends on the total ion current when the current is greater than about 1 μA, and it increases rapidly with current [22-26]. The energy spread leads to chromatic aberration, that is ions of different energies are focused at different depths. This requires that the cone angle of the ions be reduced if small diameters are to be achieved. Thus the energy spread has the effect of limiting the current density in the focal point.

1.3.2 FIB Optics

The first focusing column employing an LMIS was built by Seliger et al [13]. A schematic of the column is shown in Fig. 1.7. This is one of the simplest columns, consisting of an ion source, a single electrostatic lens, and an electrostatic deflector. Afterwards, many FIB systems were built for various applications. They can be conveniently divided into two kinds: low acceleration voltage (< 50 kV) columns without mass separation and high acceleration voltage (> 100 kV) columns with mass separators. The former is designed for applications such as mask repair, microcircuit modification, and scanning ion microscopes using a Ga LMIS. The latter is designed for applications such as ion implantation and lithography with an alloy LMIS. An example of a column with mass separator is shown in Fig. 1.8 [27]. Ions from the LMIS are focused to a crossover at an intermediate aperture by the condenser lens. Crossed electric and magnetic ($E \times B$) fields act as a velocity filter, effectively separating the ion species by mass. The $E \times B$ filter is then adjusted to allow only the desired ion species to pass through the intermediate aperture

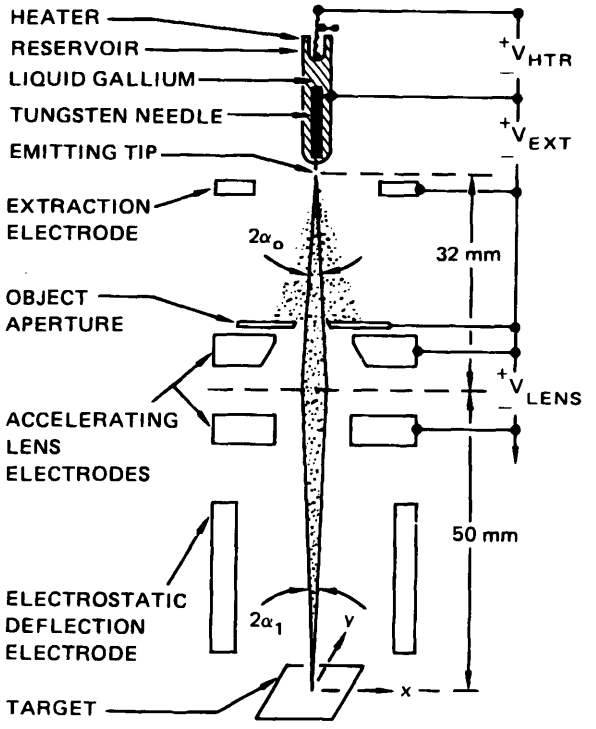

Fig. 1.7: Schematic of the low voltage focusing column without mass separator [13].

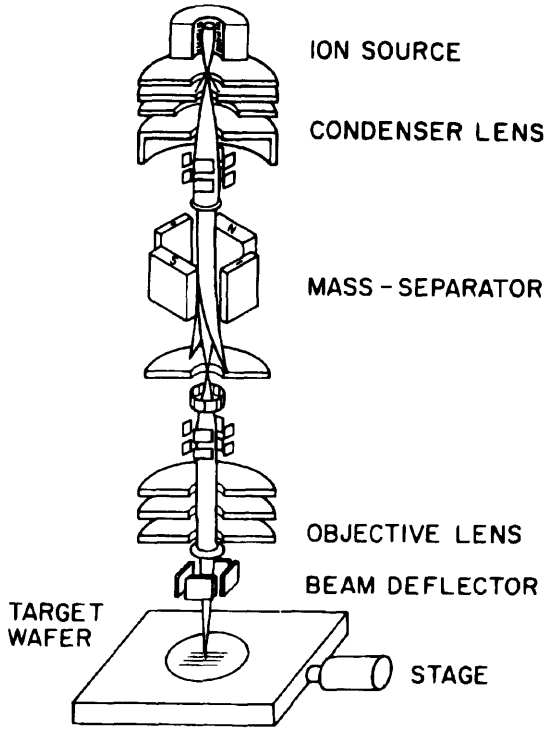

Fig. 1.8: Schematic of the high voltage focusing column with mass separator [27].

and the rest of the optical column. The objective lens then focuses the mass-selected beam onto the target. Several electrostatic deflectors are used for alignment and astigmatism correction. This type of two-lens column tends to have a shorter (~ 20 μm) depth of focus than the single-lens type (~ 100 μm) shown in Fig. 1.7 [28]. Beam current densities are usually a factor of 10 smaller since the source current is divided among the species. Different species will provide different current densities because of variations in energy spreads among the species. Also, doubly ionized species will have a favorable $\Delta E/E$ ratio (see eq. (1.7)). For example, an Au/Si alloy source will have a smaller Si^{2+} spot size than Au^{+} spot size at the same current and acceleration voltage because Si^{2+} will have a lower energy spread and higher energy due to its double ionization state [28].

The performance of an optical system is often given in terms of the size of the focused beam. It is calculated by adding in quadrature the contributions due to the source size and the lens aberrations:

$$d^2 = d_{sp}^2 + d_c^2 + d_{so}^2, \tag{1.6}$$

where

$$d_{sp} = \frac{1}{2} C_s \alpha^3, \; d_c = C_c \frac{\Delta E}{E} \alpha, \text{ and } d_{so} = M\delta. \tag{1.7}$$

C_s and C_c are the spherical and chromatic aberration coefficients, respectively, ΔE is the width of the energy distribution, E is the beam energy, α is the beam limiting aperture half angle, and δ is the virtual source size. This procedure, while fast and convenient, gives predictions for system performance which are often quite inaccurate [21]. The reason is that it does not take into account the actual current density distribution $J(r)$ at the target plane but assumes it to be uniform. Actually, $J(r)$ is often very nonuniform and the details of $J(r)$ affect both the attainable resolution of the system and the morphology of the features the beam will produce if used for milling or deposition. In order to determine the optical system performance accurately, $J(r)$ must be calculated or measured in a rigorous way. The calculation can be done in terms of the diffraction theory of aberrations or by using geometrical optics with third order aberration theory [29]. Fig. 1.9 (a) and (b) show the calculated and measured $J(r)$, respectively [30] [31]. Both of them indicate that $J(r)$ consists of a central peak and broad tails. The resolving power of the system mainly depends on the FWHM of the beam current distribution, namely the width of the central peak. However, if one is interested in, for example, deposition of materials with the FIB, then the current in the tail of the beam is important [26]. While $J(r)$ may be of the order of 1 A cm^{-2} at the peak, it will fall by 2-4 orders of magnitude in the tails. The area covered

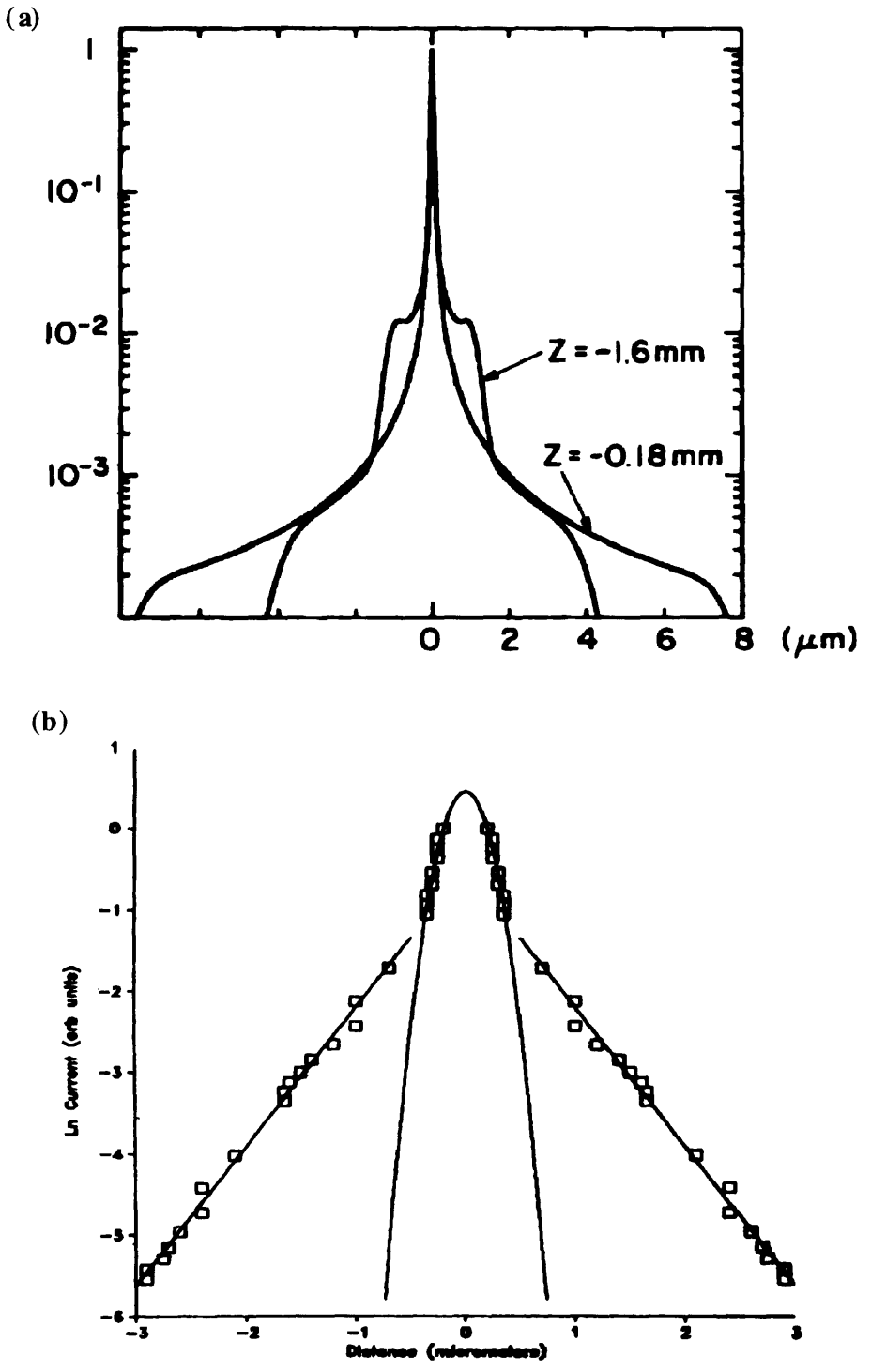

Fig. 1.9: (a) The calculated current density distribution for a FIB system at two different states of focus [30]. (b) Natural log plot of the measured current density distribution (squares) with Gaussian (center peak) and exponential (tails) fittings [31].

by the tails can be so large compared to the central peak that they will contain a significant fraction of the total beam current. This can be seen in these figures. Therefore, the long tailed beam current distribution can be the limiting factor in fabricating nanometer structures with focused ion beams similar to the electron beam proximity effect.

1.3.3 FIB Applications

Ion beam applications exploit one or more of three basic aspects of interaction between ion and matter. The desired effect of the ion beam may be produced by (1) the presence of the ion introduced into the solid, such as in ion implantation; (2) pseudoelastic collisions between energetic ions and the atoms of the target material where the momentum transfer results in displacements of the atoms, such as in physical sputtering or radiation damage; and (3) inelastic scattering of the ions with electrons in the target producing excitations which may induce chemical changes, such as in resist exposure or ion induced deposition. Incident ions will always lose energy by collision processes and eventually come to rest. The relative proportions of these effects depends on the ion species (mass), energy, in some cases arrival rate (current density), and properties of the target. These effects have been extensively studied due to the wide-spread use of ion implantation for integrated circuit fabrication. Therefore, tabulated data of ion projection range and simulation code for ion trajectories in the solids are readily available [32].

A number of secondary events occur as a result of the ion-solid interaction process. In fact, many of the ion beam techniques are driven by these secondary processes. When an energetic ion loses its energy in matter, the collisions induce emission of secondary electrons, secondary ions, photons, and sputtered neutral atoms. Secondary electrons are used for forming images in ion microscopy and secondary ions can be used for secondary ion mass spectroscopy (SIMS) analysis. Again, the yield and relative production of these secondary species depend on the primary ion beam and target material.

The above phenomena are common to all type of ion bombardment of solids. However, FIB technology has stimulated new ion beam applications in the semiconductor industry. For example, a finely focused ion beam can write arbitrary patterns on the target, enabling "maskless" implantation processes which eliminate lithographic processes. All of the FIB applications commonly utilize the benefit of "maskless" process or "high-resolution" capability of focused ion beams. The applications demonstrated so far can be grouped into six categories according to the physical interaction processes utilized. They are the following: (1) implantation; (2) milling; (3) surface chemistry (etching and deposition); (4) lithography; (5) microscopy; (6) materials analysis. Detailed discussions

of the applications are given by some articles [21], [33], [34], [35]. So, in this section, they are only reviewed briefly.

The attraction of FIB implantation is that it is a maskless resistless process, and, in addition, the dose can be varied from point to point on a wafer. Thus one can make devices side by side, each with a different dopant dose, and one can vary the doping as a function of position within a given device, (e.g., introduce a lateral gradient of carrier density).

Ion milling is a method of material removal by means of physical sputtering phenomena. The sputtering process involves the transfer of momentum to surface and near-surface atoms from the incident ions through a series of collisions within the solid target. If the ion beam impinges on the target vertically there must be enough momentum reflected from the solid to eject one or more surface atoms. Therefore, the sputtering yield S, which is defined as a ratio of the number of ejected atoms to the number of impinged ions, is a function of the angle of incidence of the ion beam as well as the mass and energy of the ions, the mass of the target atoms and the nature of the target atomic structure. FIB milling is carried out with repetitive scanning over a designated area. Arbitrary surface topology can be created by controlling the scanning pattern, scanning location, and ion dosage.

In contrast to ion milling, ion induced deposition is an additive process which is carried out by decomposing with ion bombardment metal-bearing gas molecules adsorbed on the surface of the substrate. The reactant gas, typically a metal organic compound, is

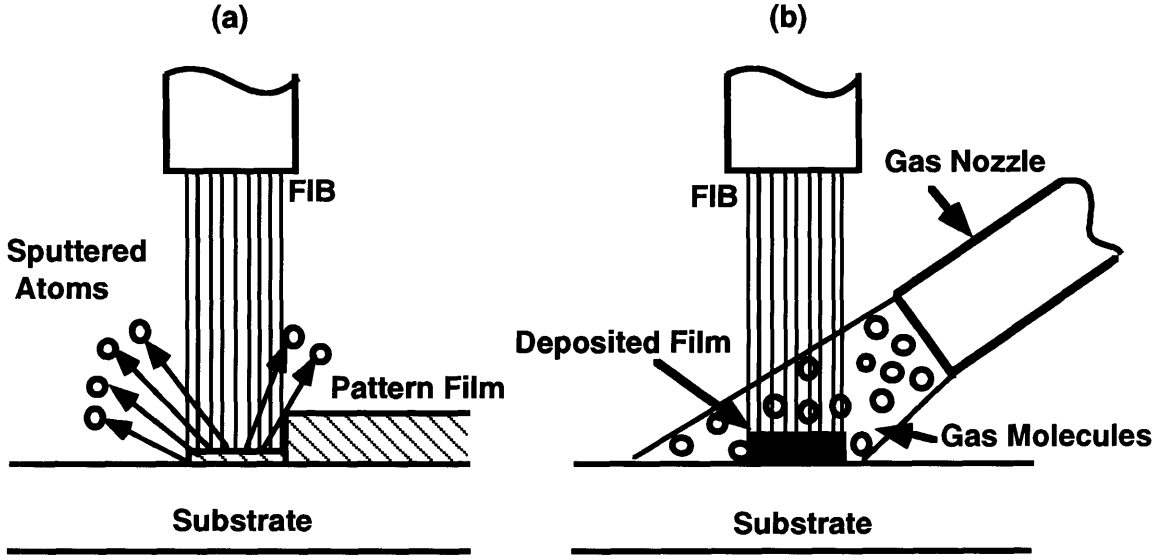

Fig. 1.10: Schematics of (a) FIB milling and (b) FIB induced deposition.

delivered through a capillary nozzle which is pointed at the surface where the ion beam is incident. The molecules decomposed by ion bombardment are desorbed from the surface leaving metal atoms and forming a thin metal film on the surface. The decomposition of the precursor gas occurs only where the ion beams irradiates. Therefore, the film shape and thickness is determined by the FIB scanning pattern and dosage.

The combination of milling and deposition by FIB is applied to repairing lithographic photomask defects and to modifying integrated circuits [36-40]. Unwanted pattern films, such as opaque defects in photomasks and misconnections or shorts in ICs are removed by FIB milling. Missing pattern films, such as clear defects in photomasks and broken lines or missing connections in ICs are added by FIB induced deposition. Fig. 1.10 illustrates these repair procedures.

FIB systems can also be used as scanning ion microscopes (SIM). Most FIB machines have a secondary electron detector. The signal from the detector is used to form an image of the target surface electrically (e.g., modulating intensities of a cathode ray tube). This imaging capability supports many of the applications discussed above. It is used to adjust the ion beam focusing when initially setting up operation, to define milled features, to align doping area to existing features on a wafer, and to locate defects to be repaired.

In a SEM, the signals can be generated from a number of electron induced processes including low energy secondary electrons, backscattered high energy electrons, cathode luminescence, x-rays, and Auger electrons, all of which carry information about target topography or chemical composition. In the case of ion beams, the signals detected are low energy secondary electrons and/ or secondary ions. Luminescence from the target has been seen as well. The secondary electron yield per incident ion is an important physical parameter in the SIM applications. The value of secondary electron yield for keV energy ions ranges between 1 - 10. However, systematic studies of the ion induced secondary electron yield for various combination of ion species and target materials are so rare that the tabulated data of secondary electron yield are either not available or unreliable.

Generally, the secondary electron emission by ion bombardment is much more sensitive to details of surface structure in the target than in the SEM because the projection range of ions in the keV energy range is quite short. Many electrons are produced in collision processes between ions and target atoms, and because of momentum conservation, the electrons excited by the ions have rather low energies. The region of interaction is quite shallow and so the number of secondary electrons escaping from the surface of the target will be proportional to the cosine of the angle between the target normal and the incident ion trajectory. Since the low energy electrons produced deep

below the surface cannot escape, SIM is especially sensitive to the surface topography. Low energy electrons will also be sensitive to the work function of the surface [41]. The SIM secondary electron signal will thus depend on the chemical nature of the surface as well as its morphology. This chemical effect will vary with target material, but there is invariably a secondary electron yield difference between oxides and clean elemental surfaces. The yields for oxides are always higher than for metals. It is understood from two qualitative arguments [42]: (1) The mean free path of secondary electrons is larger for oxides than for metals. Hence the escape depth and the yield will be larger; (2) The work function of oxides is smaller than for metals. More low energy electrons will be able to surmount the surface barrier. This effect will increase the secondary electron yield.

Another feature differentiating SIM from SEM is the greater sensitivity of an incoming beam to the crystalline structure of the sample. In a crystalline sample it is possible for the primary ions to channel if the orientation of the crystal is aligned with the beam. In this case, the ions travel between the columns of atoms and their range can be quite large. Since a longer range implies less interactions (per unit length) between ion and sample, the number of secondary electrons produced will be lower if the sample is oriented in certain directions relative to the beam. This effect induces image contrast depending on small changes of the angular orientation of the sample, which is called "channeling contrast". The channeling contrast is being used for the observation of the grain structure

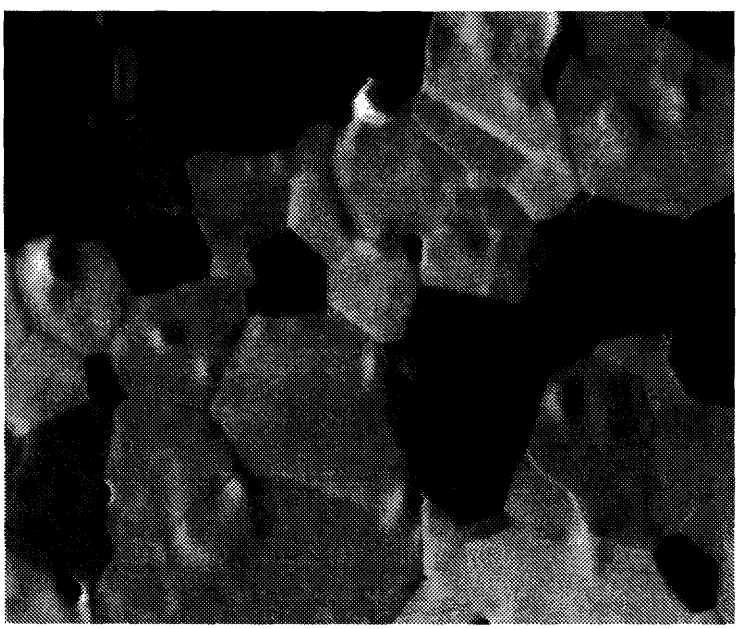

Fig. 1.11: SIM image showing channeling contrast of Al grains [44].

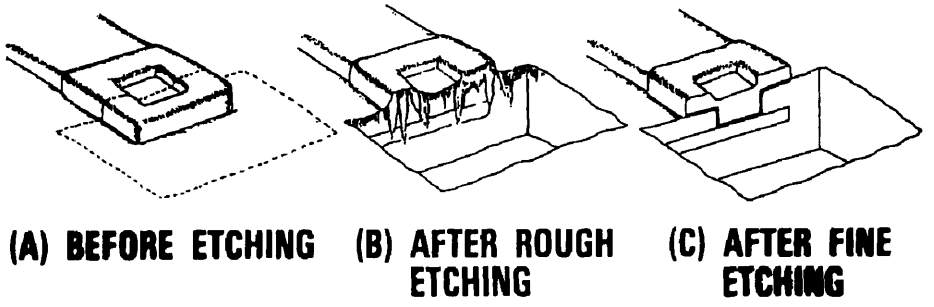

Fig. 1.12: Illustration of procedure to form cross sectioning by FIB [44].

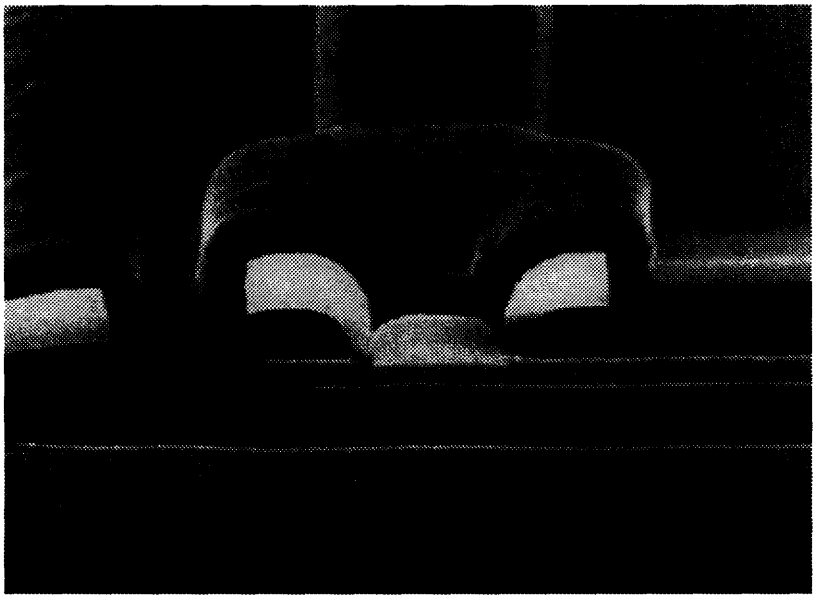

Fig. 1.13: Cross sectioning SIM image of microelectronic device [44].

of aluminum in microcircuit devices which relates to electromigration phenomenon [43]. An example of the channeling contrast of aluminum grain observation is shown in Fig. 1.11.

One of the SIM applications that is widely adopted in the semiconductor industry is cross section observation [43]. This is done by the following procedure (see Fig. 1.12): (1) locate an area to be sectioned by SIM; (2) ion mill a depression to form cross section that can be observed on one end wall of the depression; (3) tilt the sample and observe the wall by SIM. Fig. 1.13 is a SIM image of the cross section of a microdevice. This cross

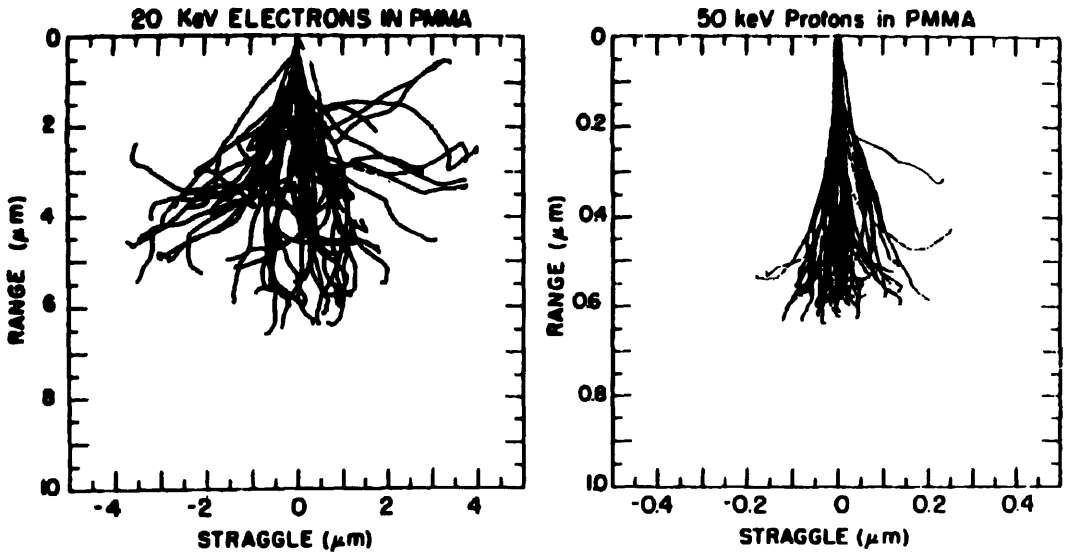

Fig. 1.14: A Monte Carlo simulation of the trajectories of ions (50 keV protons) and electrons in PMMA. Note the difference in scale and the fact that the ions scatter far less than electrons [45].

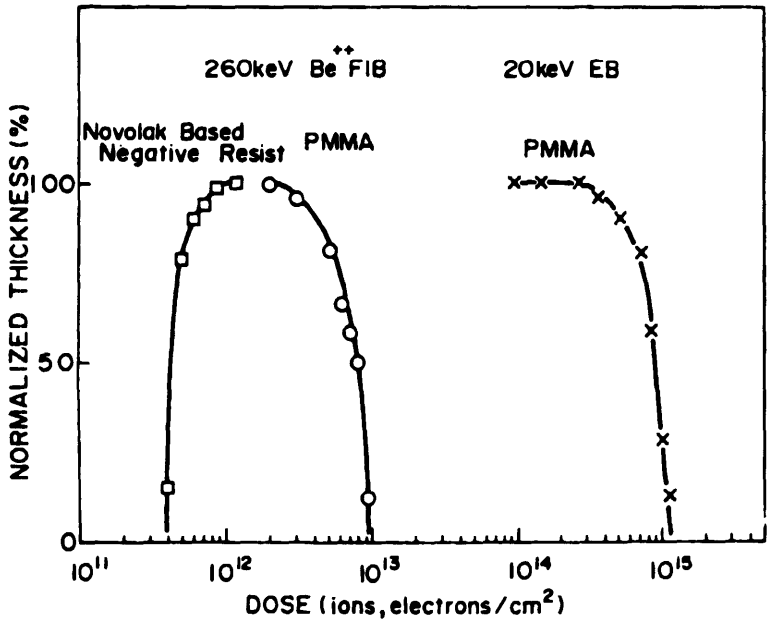

Fig. 1.15: Exposure characteristics of PMMA and negative novolak resist by ions and electrons. The vertical axis shows the percentage of thickness remaining after development [46].

sectioning method is utilized for failure analysis and process monitoring in the IC manufacturing industry.

As mentioned before, FIB lithography by resist exposure is another important FIB application because of the absence of the proximity effect. When electrons are incident on a solid, they tend to scatter their energy into a relatively large volume (of one to several micrometers dimensions). This is because they are incident on a medium largely filled with particles of equal mass, so that energy transfer in scattering is maximum. Ions, on the other hand, scatter their energy over a relatively small volume close to the point of entry. Fig. 1.14 shows electron and ion trajectories in PMMA calculated by a Monte Carlo method [45]. This indicates that the scattering of ions in resist is far less than that of electrons. In addition, since exposure of resist is produced by the energy deposited by the incident particles, the resist sensitivity of ions, which is determined by the number of molecules of resist transformed by the incident particles, is in general about two orders of magnitude greater than that of electrons, as shown in Fig. 1.15 [46]. The high resist sensitivity of ions results in exposure throughputs competitive with those of the other lithographic methods. For example, resist such as PMMA are about two orders of magnitude more sensitive to ions than to electrons. On the other hand, the current density of most commercial electron beam systems (10-100 A cm^{-2}) is about two orders of magnitude higher than that of ion beams (0.4-4 A cm^{-2}). Thus, these two effects approximately cancel, and exposure times are expected to be comparable for resists like PMMA. A number of experimental results of FIB lithography have been reported to exhibit the capability of a few tens of nanometer resolution [10]. The minimum width lines exposed in PMMA are in the 12-15 nm range [9]. Apparently, lighter ions are preferable for exposing fine features in resist because of longer projection range. Most of the reported results were exposures done with Be and Si ions, which are relatively light ions that can be extracted from LMIS. However, some reports showed 15 nm resolution with relatively heavy Ga ions [9]. In this case, very thin layer of resist on the substrate (< 0.1 μm) are required.

1.4 Spatial Phase Locking Method

Pattern integrity by particle beam lithography is often limited by the stitching error, as mentioned in section 1.2. In commercial SEBL systems the specification on the field stitching error is typically $3\sigma \approx 75$ nm, a factor of 10 poorer than the minimum beam diameter (< 10 nm). There are many causes of stitching error including the following: (1)

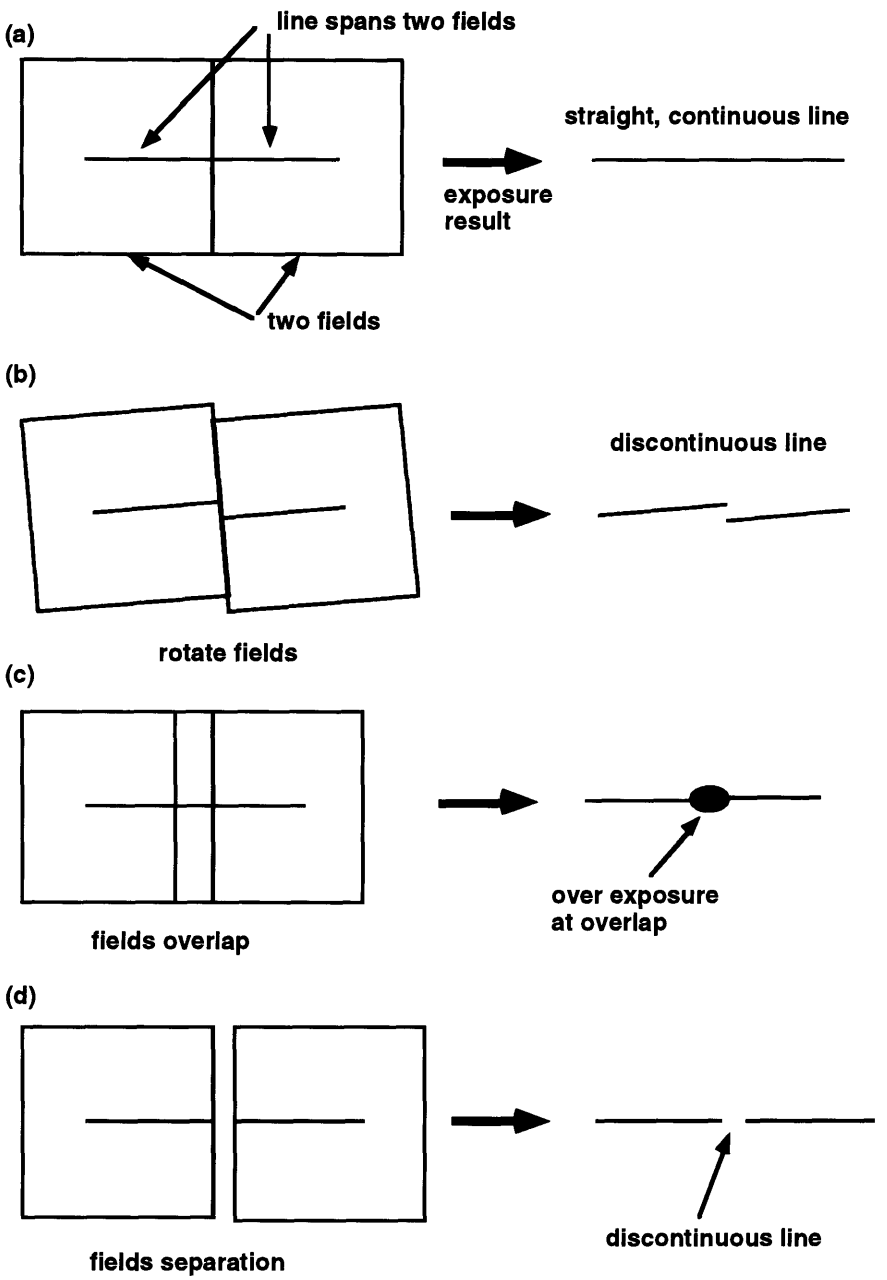

Fig. 1.16: Illustration for explanation of field stitching (a) and three types of stitching errors (b)(c)(d) [6].

Miscalibration of scanning field magnification with respect to the stage coordinate system; (2) Rotation of scanning field axes with respect to the stage motion axes; (3) Errors in the detection of the stage position by laser interferometer system; (4) Drift of the stage due to thermal expansion; (5) Drift of electrical sources also due to thermal effects. At least three types of stitching errors can arise, as shown in Fig. 1.16. Fig. 1.16(a) shows the correct placement of two fields and a straight, continuous line that spans two fields. The next three figures (b), (c), (d), show different types of stitching errors. When the fields are rotated with respect to the stage axes, the exposed line is discontinuous as shown in (b). If the scan field length scale is not identical to that of the stage, the fields can overlap at their boundaries, resulting in overexposure and pattern error, as shown in (c). If the scan fields do not abut, line can be discontinuous, as shown in (d).

As has been shown, the identifiable sources of distortion are quite varied (thermal, electromagnetic interference, etc.). It would be extremely difficult to account for all sources in a model in order to eliminate the unwanted effects that they give rise to. These difficulties arise because the important parameter, sample-to-beam-displacement, is not monitored directly and one has to rely on secondary referencing by measuring the position of the stage with an interferometer (actually, the position of the stage is not being measured, but the position of the mirrors attached to it) and extrapolate from this measurement the information needed. If the beam can be made to interact with the sample in such a way that information is provided about their relative position, the problem can be solved. An approach that constitutes such a solution has been proposed, which is called "spatial-phase-locking" method [6] [47] [48] [49]. The fundamental idea is to provide a spatially coherent fiducial reference on the sample, preferably in such a way that the control computer maintains continuous tracking of beam location.

The fiducial reference used in spatial-phase-locked beam lithography (SPLBL) consists of a grid with long-range spatial-phase coherence created by interferometric lithography on top of the resist to be imaged. The interferometric lithography technique uses optical standing wave produced by intersecting two laser beams as an exposure source [6] [49]. Fig. 1.17 shows a configuration of the interferometric lithography system used at MIT [6]. A grid fabricated by this technique has long-range spatial phase coherence and so can serve as a global fiducial reference in SPLBL.

The grid will modulate a signal from the surface due to the difference of secondary electron yields among the materials consisting of the grid, which varies as a function of beam position. This signal can then be processed to extract the appropriate positional information and fed back into the beam deflection subsystem to correct for any deviation

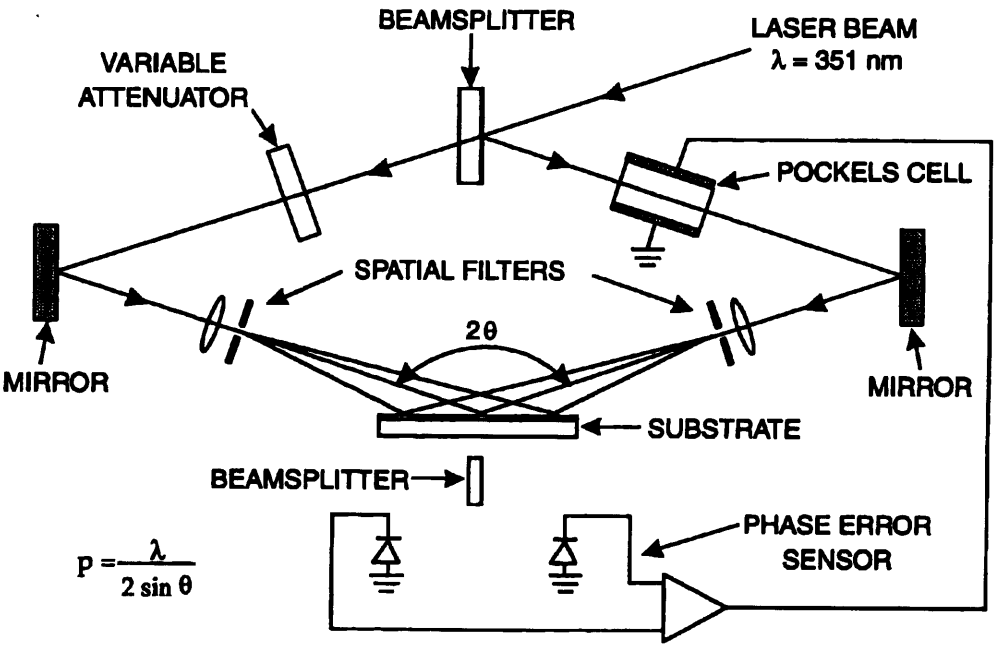

Fig. 1.17: Configuration of interferometric lithography system [6].

from the intended beam position. In this way, a feedback loop will be put in effect, which will actively correct for any one of the multitude of errors that can arise in the system.

Fig. 1.18 illustrates one possible configuration in which the grid is created by interferometric lithography in thin resist on top of a thin aluminum film. The function of the conducting film is to carry off charge. Both the resist grid pattern and the aluminum film are easily penetrated by the high energy incident beams. As the electron or ion beam writes a pattern, the secondary electron yield is modulated as the beam moves from the conductor to the insulator. These secondary electrons, when collected, provide information on beam location which can be used to compensate for beam drift, or other type of position error. Preliminary tests of spatial-phase-locked electron beam lithography have been reported [48]. Results of these tests show that a pattern placement precision of 1 nm will be possible.

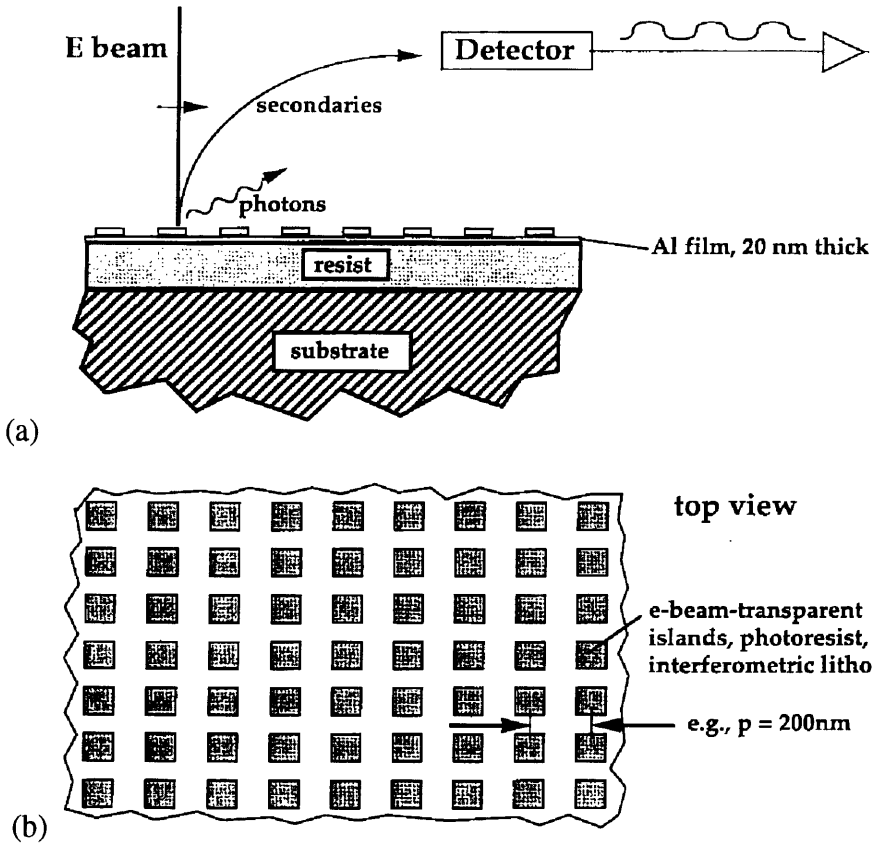

Fig. 1.18: (a) Cross-sectional schematic of a global fiducial grid configuration. (b) Top view of the global fiducial grid [6].

1.5 Objectives

Principle of spatial-phase-locked beam lithography has been applied to electron beam system and its effectiveness confirmed [48]. The main objective of this research is to investigate the feasibility of the spatial-phase-locking method when the principle is applied to focused-ion-beam lithography. It is very important to determine whether the secondary signal acquired by FIB irradiation over the fiducial grid carries enough information about the beam position. In other words, whether the signal from FIB induced secondary electrons can be used as a reference of beam position, or not. Difference in metal and polymer secondary electron yield strongly influence the secondary electron signal modulated by the grid. The materials must be chosen to maximize this difference.

In this research, secondary electron yield induced by FIB irradiation has been investigated. The target materials were aluminum as a metal sample, PMMA as a polymer sample, and silicon as a reference. Aluminum and PMMA are potential candidate materials

to form a fiducial grid structure. The ions used were 120-240 keV Si^{2+}, which could be used as a source of FIB lithography. Au^{2+} ions were also used in some cases for comparison. The secondary electron yields for various energies and materials were measured as a function of time to check their ion dose dependence. This information can be utilized for analyzing the surface condition of the target materials. Also the density of ion irradiation was varied. Finally, possible contrast that will be obtained from a fiducial grid will be discussed.

2. Experiments

This chapter will cover the experimental equipment and procedures for the measurement of the focused-ion-beam induced electron emission yield. The focused-ion-beam (FIB) system that used in this study will be described here. Then, the method for measuring the electron yield and the sample preparation procedure also will be discussed.

2.1 Focused Ion Beam System

The FIB system used in this experiment is shown in Fig. 2.1. This machine is designed to perform FIB implantation and lithography with acceleration voltage from 30 kV to 150 kV. The configuration of the system is quite similar to Fig. 1.8. The ion beam column consists of a liquid-metal ion source, a set of electrostatic lenses, an $E \times B$ mass separator, a beam blanker, deflection plates, and a secondary electron detector. In the present work, a Au/Si alloy source is used as a source of silicon and gold ions. Typical mass spectrum of a Au/Si alloy source is shown in Fig. 2.2, which is obtained by sweeping either the E or B field in the $E \times B$ mass separator and measuring the current passing through the aperture [50]. This spectrum indicates that doubly charged silicon ions (Si^{2+}) are the dominant species in silicon ions extracted from a Au/Si alloy source. Si^{2+} or doubly charged ions in general are preferable for implantation and lithography applications because higher energy beams can be achieved compared to singly charged ions. The ultimate beam diameter of Si^{2+} at the target plane is about 0.1 μm, which is confirmed by means of the resolution of the SIM image.

SIM images are formed by raster-scanning the ion beam over a sample. A saw-tooth-wave signal is supplied to the deflector plates and secondary electrons induced by the incident ions are detected with a channel electron multiplier. The amplitude of the saw-tooth signal determines the size of the scan field. The smaller the scan field size the larger the image magnification. The time to scan a field once (a frame) is kept constant by using a fixed period saw-tooth. So at a fixed beam current, the number of incident ions per frame is also constant. The average current density of ions (ions/unit area) then can be varied by changing the scan field size or area.

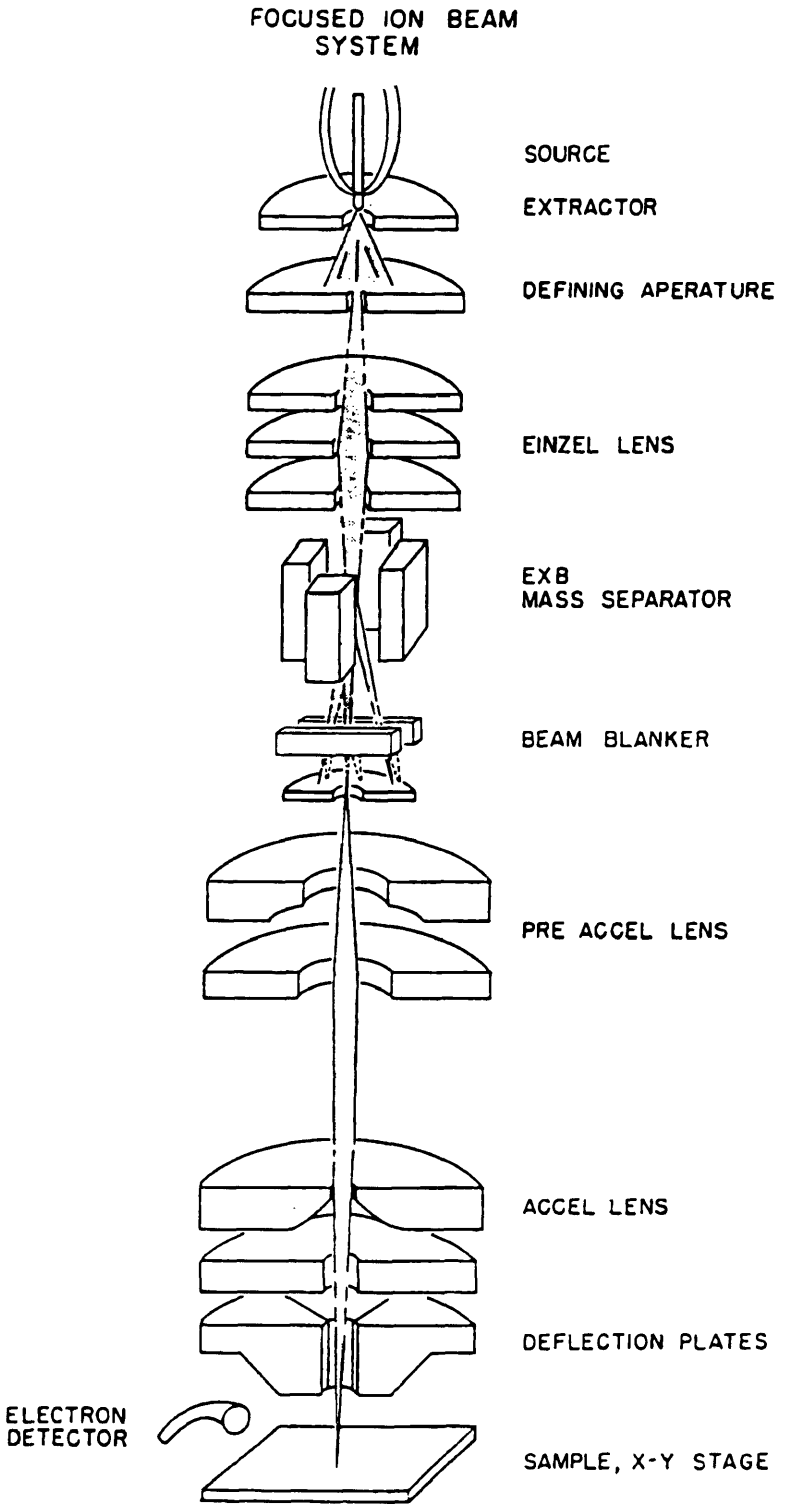

Fig. 2.1: Schematic of focused ion beam system used in this research.

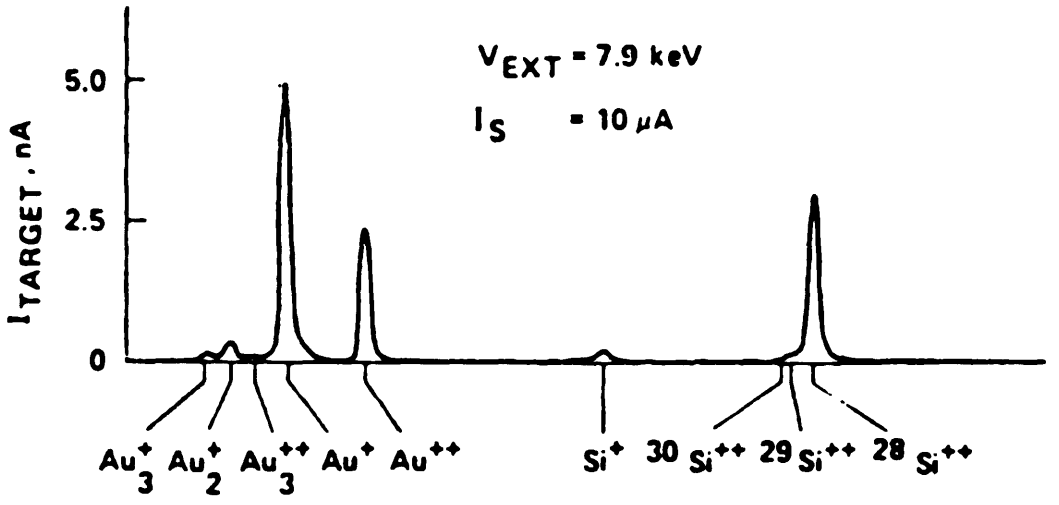

Fig. 2.2: Typical mass spectrum of ions extracted from Au/Si alloy source [50].

The system is evacuated with an ion pump and a turbo molecular pump and operates in a high vacuum condition (< $5\text{x}10^{-7}$ torr). An airlock is provided for sample exchange. At this vacuum level, the surface of the sample is exposed to residual gas, such as water vapor, oxygen, and carbon oxide, and still oxidized if the surface is pure. As will be shown later the vacuum level greatly influences the secondary electron yield.

2.2 Secondary Electron Yield Measurement

Secondary electron yield γ is defined by the number of emitted electrons per incident ion. In this work, $\gamma$is measured by the quotient method [42], which directly refers to the definition of the secondary electron yield as the quotient of the secondary electrons to the number of incident ions. Consequently, γ may be determined from the ratio of two currents, namely emitted electron current and incident ion current. It can be expressed by

$$\gamma = z\frac{-I_e}{I_{ion}}, \tag{2.1}$$

where I_e is the current of emitted secondary electron and I_{ion} is the current of impinged ion of charge state z. However, it is difficult to measure the secondary electron current directly. Typically, total target current, that is the sum of the two currents, is measured

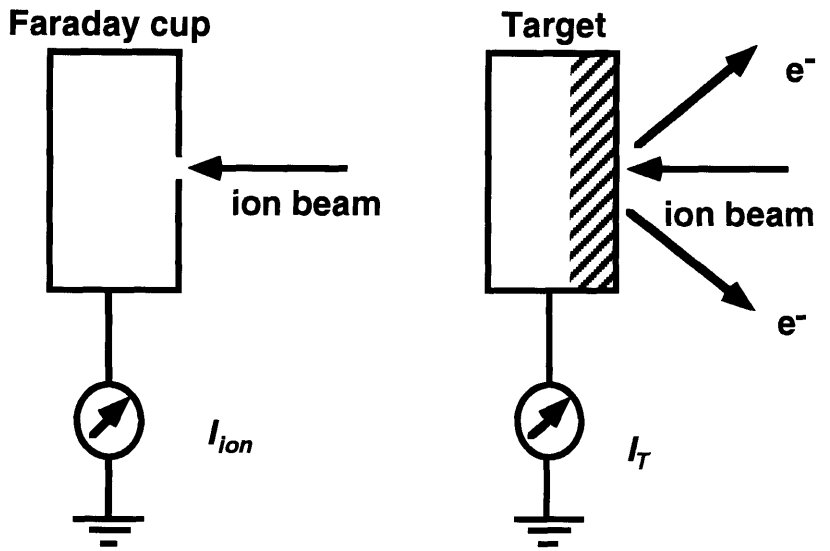

Fig. 2.3: Schematic of the quotient method for secondary electron yield measurement.

instead of I_e. Fig. 2.3 illustrates the principle of the quotient method using measurements of the total target current and the incident ion current at the Faraday cup. In this case, γ may be determined as

$$\gamma = z\frac{I_T - I_{ion}}{I_{ion}}, \tag{2.2}$$

where I_T is the total target current. In this research, secondary electron yields are calculated using this formula.

In order to realize this method, a special sample holder was manufactured, which is isolated electrically and can be connected to a pico-ampere meter via a vacuum feedthrough. Furthermore, the Faraday cup is fabricated on this holder so that the incident ion current is readily monitored by a short stage movement.

2.3 Sample Preparation

In this work, three kinds of target materials are used: silicon, aluminum, and PMMA. No special consideration was taken to prepare the samples

B-doped, p-type, (100) silicon wafers are used as the silicon sample. They are also used as substrates for aluminum and PMMA samples.

Aluminum samples are prepared by electron-beam deposition onto the silicon wafers. The thickness of the deposited aluminum film is about 2000 Å for all samples used in this experiment. Mean escape depth of low-energy secondary electrons is typically 5-20 Å for metals and 30-300 Å for oxides [51] [52]. Thus the thickness will not influence the measurements of secondary electron yield. The electron-beam deposition apparatus is evacuated by a cryo-pump down to a base pressure of the 10^{-6} torr range. Al deposition is carried out under this vacuum condition. The Si wafer substrate has a very flat, polished surface. Therefore, the Al film deposited on the Si is so flat that the effect of topography on secondary electron yield is negligible. This allows stable measurements which are not affected by the surface topography.

PMMA films are spin-coated on the silicon wafers with the thickness of about 2000Å for all samples used in this experiment. The PMMA samples are then pre-baked in an oven at 90°C for 20 minutes.

3. Results and Discussion

Yields of FIB induced secondary electron from Si, Al, and PMMA were measured as a function of irradiation time. The dependence on the average current density was also investigated. The ion beam used was Si^{2+} with energies of 120 - 240 keV. Also, Au^{2+} beam was used for an Al target. In this chapter, the results of the measurements will be described. Then, a discussion with emphasis on the surface condition of the target will be given. Finally, the contrast that may be obtained from a fiducial grid will be discussed.

3.1 Results on Si Target

While a Si^{2+} focused ion beam was scanned over a Si sample, target current was monitored with a picoampere meter. Secondary electron yield can be calculated using eq.(2.2). Fig. 3.1, 3.2, and 3.3 show the measured secondary electron yields for the beam energies of 120 keV, 180 keV, and 240 keV as a function of irradiation time for various scanning fields. Each line corresponds to a different scanning field which is referred to as 2x, 4x, 8x, 16x, or 32x. 2x is the largest scanning field and 32x is the smallest. The relation between these numbers and actual scan field is summarized in Table 3.1. It must be noted that the size of the scan field (or scanning magnification) for different beam energies varies since the voltage applied to a deflector remains constant for the same magnification. The ion beam current used was 40 pA for all measurements, as measured by the Faraday cup on the sample holder. As mentioned in a previous chapter, the time to scan a frame is kept constant (~ 19 msec). Thus, the average current density over the scanning field is calculated by I_{ion} / A, where I_{ion} is beam current and A is area of the scanning field.

There are several points to note in these graphs: (1) In all the graphs, curves for higher magnifications (32x and 16x) show a decrease in the yields with time. Especially, the 32x curves which rapidly drop and then level out at the lowest values; (2) The slope of the drop for higher energy ion incidence is steeper than that for lower energy ion incidence; (3) In all the graphs, the curves for lower magnifications (8x, 4x, and 2x) show a very

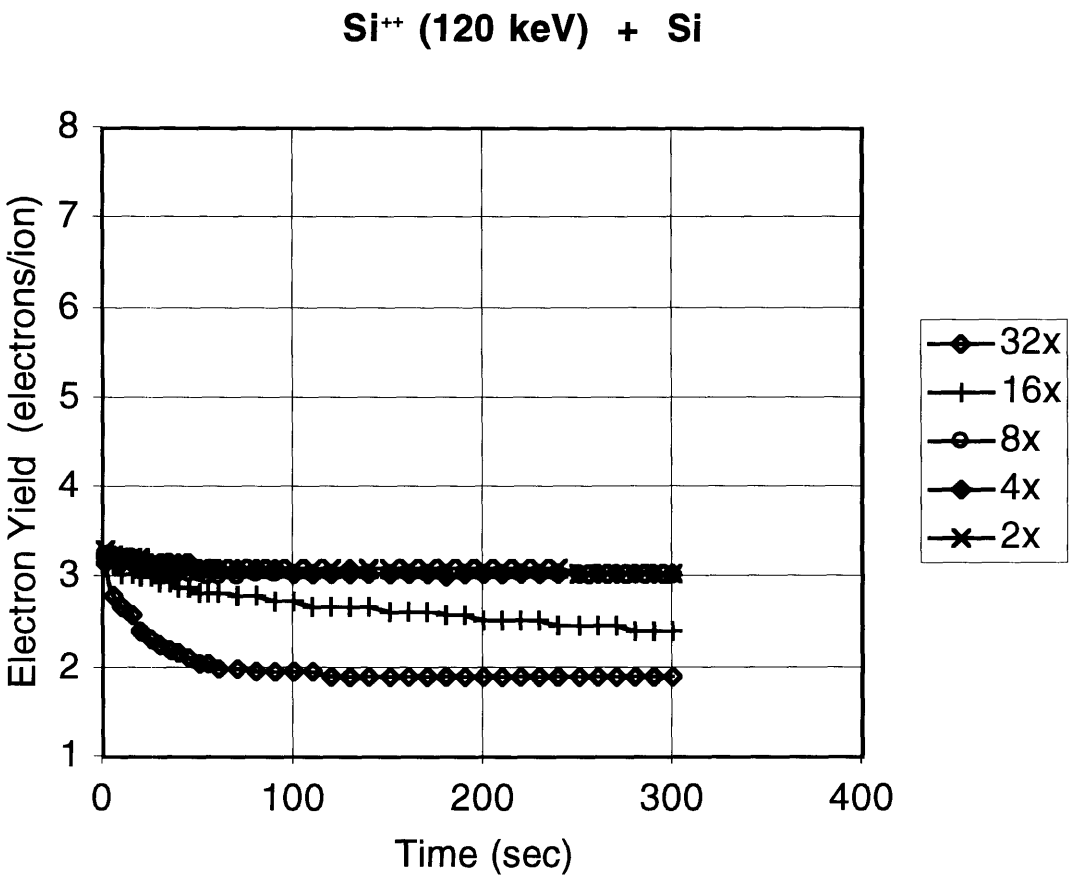

Fig. 3.1: Secondary electron yields from Si induced by 120 keV Si^{2+} as a function of irradiation time. Each line corresponds to a different scanning magnification (see Table 3.1).

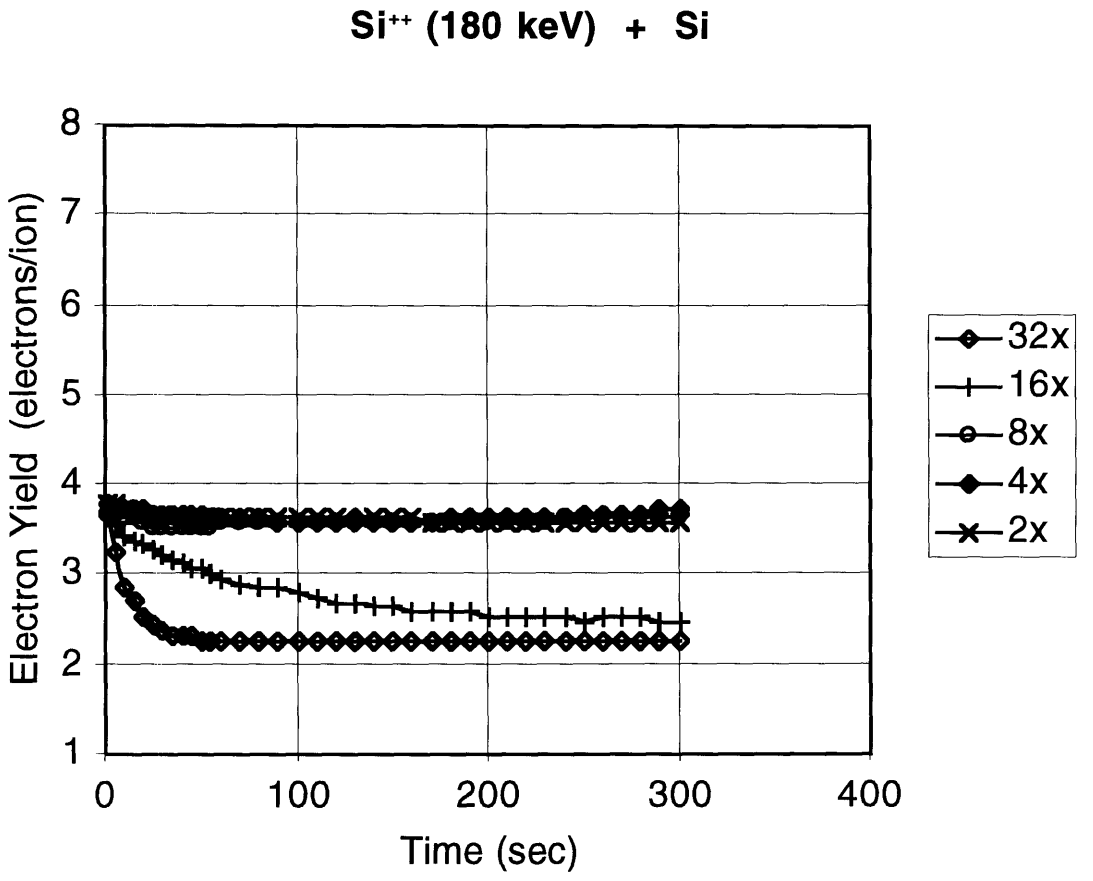

Fig. 3.2: Secondary electron yields from Si induced by 180 keV Si^{2+} as a function of irradiation time. Each line corresponds to a different scanning magnification (see Table 3.1).

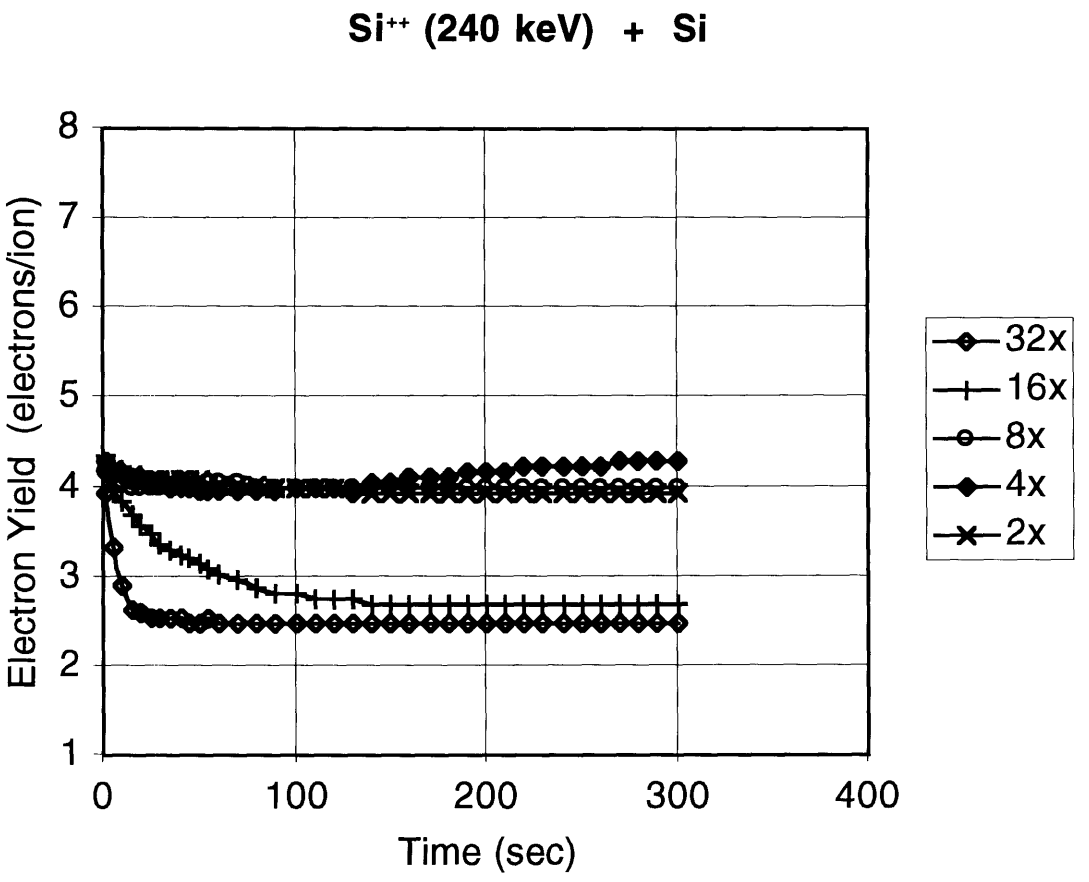

Fig. 3.3: Secondary electron yields from Si induced by 240 keV Si^{2+} as a function of irradiation time. Each line corresponds to a different scanning magnification (see Table 3.1).

	2X	4X	8X	16X	32X
120 keV	133 × 133	67 × 67	33 × 33	17 × 17	8.3 × 8.3
180 keV	89 × 89	44 × 44	22 × 22	11 × 11	5.6 × 5.6
240 keV	67 × 67	33 × 33	17 × 17	8.3 × 8.3	4.2 × 4.2

Table 3.1: Relation between scanning magnification and field size (in μm) for various beam energies.

small, rapid decrease, then stay almost constant; (4) All five curves in each graph start at almost the same value; (5) The initial (time≈0) yield increases with the beam energy; (6) The yield at longer time increases with the beam energy.

These features of the secondary electron yield can be explained by sputtering effects and the probable surface condition of the target. It is known that a native oxide film grows on silicon when it is exposed to air. The typical thickness of the native oxide is 5 to 50 Å [2]. Therefore, the surface of the Si targets is considered to be covered by thin SiO_2. The secondary electron yield of oxide is generally much higher than that of metal, as mentioned in chapter 1. This general theory can be applied to semiconductor materials [42]. The explanation given by Dekker is as follows [53].

A secondary electron produced at a certain depth x with a given energy E_0 may undergo the following types of interactions: (i) interaction with lattice electrons; (ii) interaction with lattice vibrations. The energy of a secondary electron decreases through these interactions. A minimum value of energy required to escape from the surface E_{min} is $E_{min} = E_F + \phi \approx$ several eV for metals, and $E_{min} = \chi \approx 1$ eV for insulators, where E_F is the Fermi energy, ϕ is the work function and χ is the electron affinity of the crystal. For metals, (i) refers essentially to the interaction with the conduction electrons. This is a dominant energy loss process in metals. As a result of the strong interaction between secondaries and the conduction electrons, and the relatively high average energy loss suffered by the secondaries in such collisions, the secondary electron yield of metals is in general small. In insulators the density of electrons in the conduction band is so small that their presence may be neglected. This leaves, as far as (i) is concerned, only the possibility

of energy losses due to excitation of electrons from the filled band. For such an excitation process, energies of the order of several eV are required. Thus if E_e is the minimum excitation energy involved, the interaction of type (i) do not occur for secondaries of energies below E_e. Therefore, the escape mechanism for insulators is determined by the interaction with lattice vibrations. From the fact that in a collision with the lattice an electron of several eV energy loses on the average about 0.1 eV or less, it will be evident that relatively high yields may be expected for insulators. In semiconductors, the upper filled band is separated from the conduction band by only about 1 eV. Thus, electrons with energy > 1 eV are likely to lose their energy by exciting lattice electrons from the filled band into the conduction band. This implies that the secondary electron yield for such materials should be relatively small and of the same order as for metals.

Consequently, at the beginning of ion irradiation, the measured secondary electron yield probably represents the value for SiO_2. However, during the ion bombardment the surface atoms are removed due to sputtering. As SiO_2 is sputtered the surface becomes increasingly pure Si. According to Dekker's explanation, the secondary yield for SiO_2 is greater than that of Si. Thus the secondary yield will decrease with time, because the composition of the surface changes from SiO_2 to Si with time due to the sputtering effect induced by incident ions. This is in agreement only with the higher magnification cases observed. Since the sputtering rate that is defined by the number of atoms removed per cm^2-sec is proportional to the ion current density, the lower magnification results in relatively slower sputter removal rate because of the lower current density, but still sputtering will occur. Accordingly, it is expected that the secondary yield even for the lower magnifications such as 8x, 4x, and 2x, decreases gradually with time. However, the curves for such magnifications do not show decreases but stay at almost constant value. This can not be explained by the effect of sputtering. In these cases, surface oxidation by residual gases during the ion irradiation may explain the results.

The arrival rate of residual gas molecules onto the surface can be calculated by the following formula [54],

$$N = \frac{p}{\sqrt{2\pi mkT}}, \tag{3.1}$$

where N is the arrival rate of gas molecules for a gas of molecular mass m at temperature T and pressure p. This may be rewritten as,

$$J_{gas} = (3.513 \times 10^{22})(MT)^{-\frac{1}{2}} p, \tag{3.2}$$

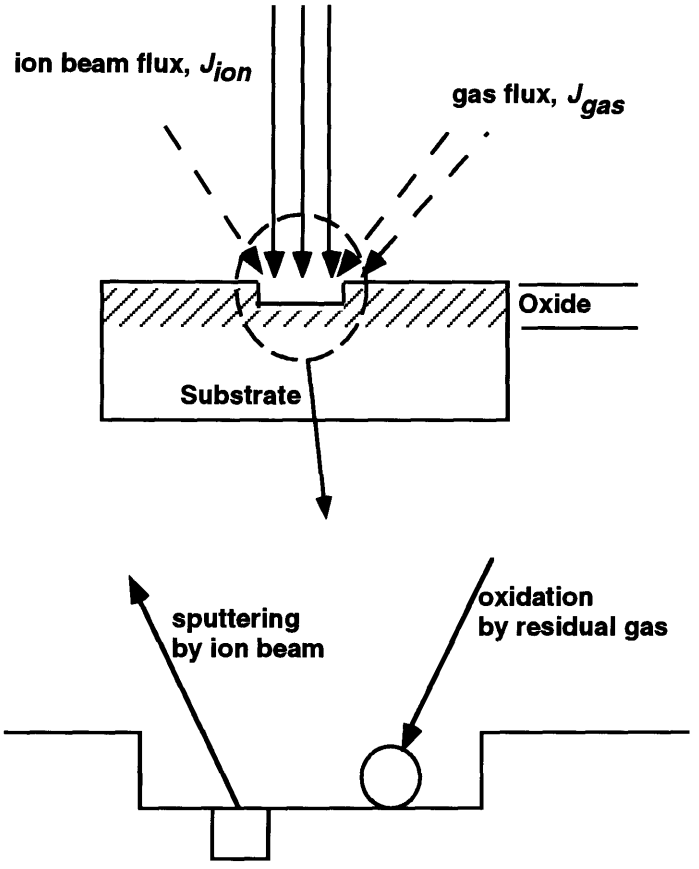

Fig. 3.4: Illustration of two competitive processes: sputtering and oxidation.

where J_{gas} is the arrival rate of gas in molecules cm^{-2} sec^{-1}, M is the molecular weight in gram $mole^{-1}$, T is in K, and p is in torr. Possible effects of residual gas, such as the surface oxidation, can be estimated using this equation.

When the current density of the incident ion beam is low and the arrival rate of residual gases, such as H_2O, CO, and O_2, at the surface of the target is high, the surface oxidation progresses as quickly as oxide is removed by sputtering. Thus the two phenomena, sputtering and oxidation, are considered to be competitive processes as illustrated in Fig. 3.4. The sputter removal rate is evaluated by (J_{ion} S) in atoms/cm^2 sec, where J_{ion} is the current density in ions/cm^2 sec and S is sputtering yield in atoms/ion. The oxidation rate is evaluated by (J_{gas} Rox), where J_{gas} is the flux of residual gases in molecules/cm^2 sec and R_{ox} gives the reaction probability which is defined by ratio of the number of oxidized atoms and the number of residual gas molecules which arrived at the surface. The tendency of the secondary yield versus irradiation time may be determined by competition between these processes. The experimental results indicate that the oxidation

process is faster than sputter removal rate keeping the surface of the targets mostly in an oxidized state. Detailed discussion using this evaluation procedure will be presented later.

The energy dependence of secondary yields is generally governed by the inelastic stopping power of the incident ions in the target, since secondary yield γ is predicted to be proportional to the stopping power [42]. For ion energies below the maximum of the stopping power, semi-empirical theory predicts that $\gamma \propto \sqrt{E_{ion}}$, where E_{ion} is energy of the incident ion beam[42]. The stopping power of Si ions in Si and SiO_2 targets will have a maximum at $E_{ion} \approx 20$ MeV according to the computation using TRIM simulation software [32]. Thus for the energy range used in this experiment, secondary yield is proportional to the square root of the beam energy. This agrees qualitatively with the observed results.

3.2 Results on Al Target

The secondary electron yield of an aluminum target was also measured with exactly the same method as described in the previous section. Some of the results are shown in Fig. 3.5, 3.6, and 3.7.

In these graphs, there are some common features with the results for Si targets, but also some considerable differences. The common features are as follows: (1) for the highest magnification (32x, highest current density) secondary yields show decreases with time; (2) for the lowest magnification (2x, lowest current density) secondary yields show little change with time; (3) secondary yields at the beginning (time $\approx$ 0) indicate almost the same value for all magnifications in each graph and the value increases with ion energy. All these phenomena may be explained by the surface condition of targets due to the competitive process between oxidation and sputtering as in the case of silicon samples. The different features are as follows: (1) for intermediate magnifications, (16x and 8x for 120 keV, 8x 4x for 180 keV and 240 keV) curves increase with time and do not saturate in the period measured; (2) 32x curves for all energies and 16x curve for the case of 240 keV show a small bump at time = 5-40 sec unlike the curves for the Si target where yields decrease monotonically with time; (3) for 32x curves more time is required to reach saturation level than in the case of Si targets, and the difference of the yields at the beginning and at the saturation level is larger than the case of Si. These differences are due to the difference of the characteristics of aluminum and silicon.

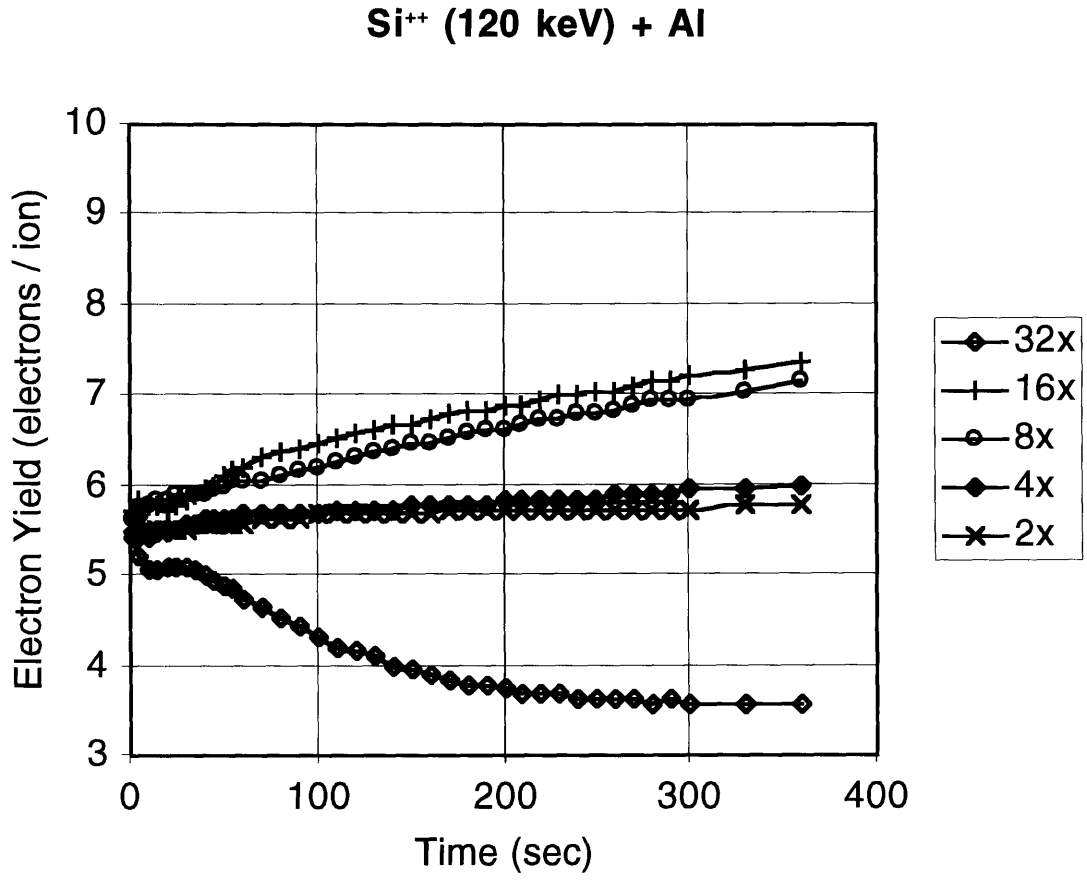

Fig. 3.5: Secondary electron yields from Al induced by 120 keV Si^{2+} as a function of irradiation time. Each line corresponds to a different scanning magnification (see Table 3.1).

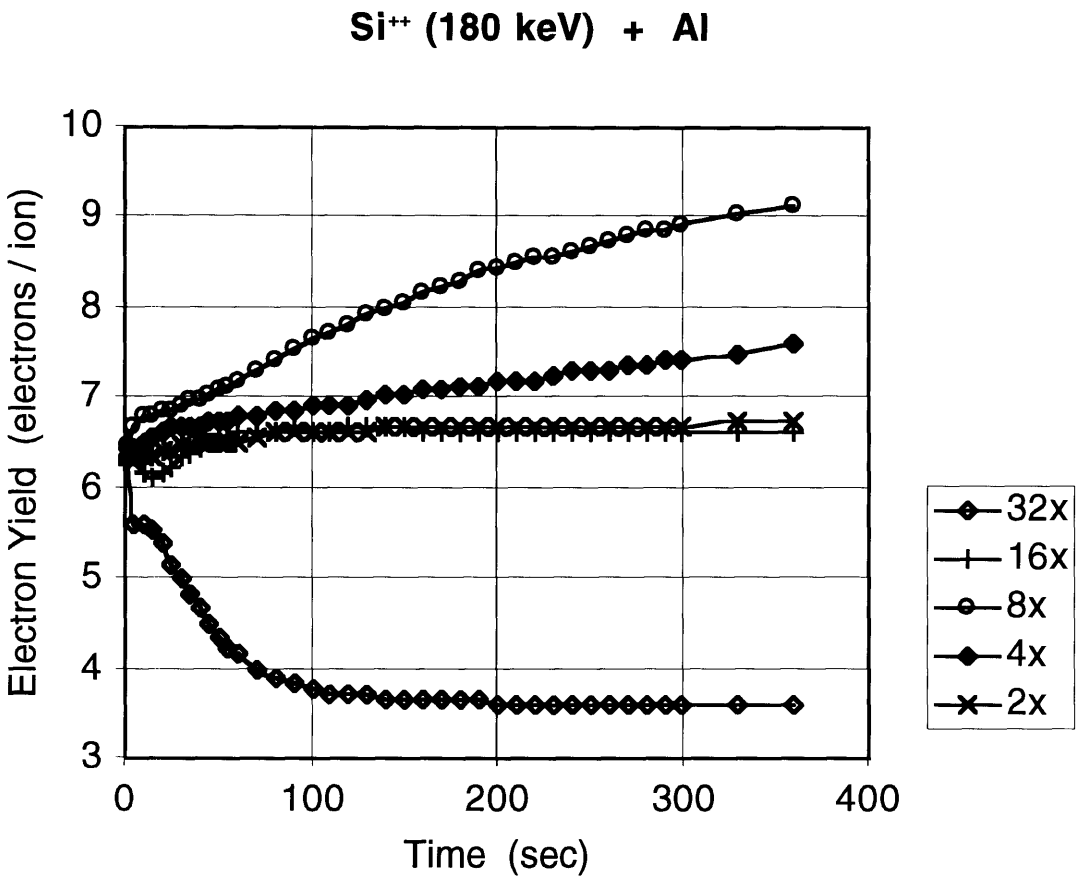

Fig. 3.6: Secondary electron yields from Al induced by 180 keV Si^{2+} as a function of irradiation time. Each line corresponds to a different scanning magnification (see Table 3.1).

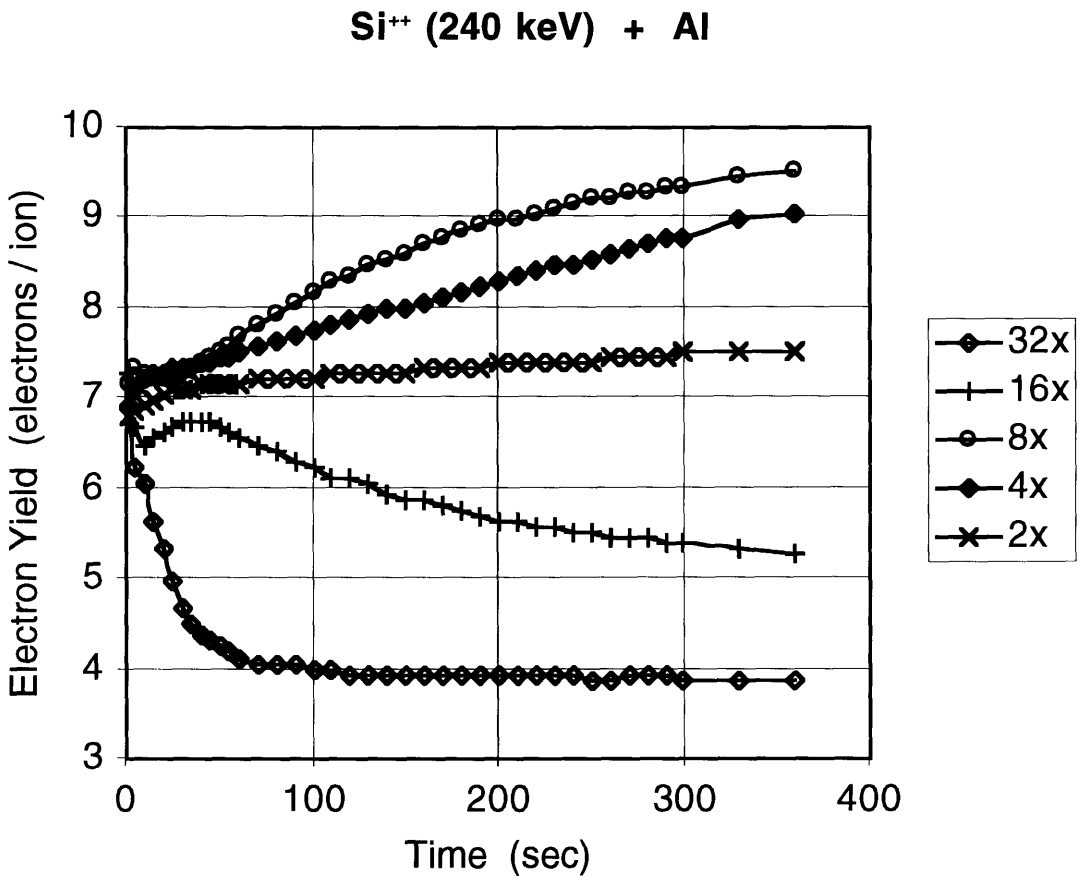

Fig. 3.7: Secondary electron yields from Al induced by 240 keV Si^{2+} as a function of irradiation time. Each line corresponds to a different scanning magnification (see Table 3.1).

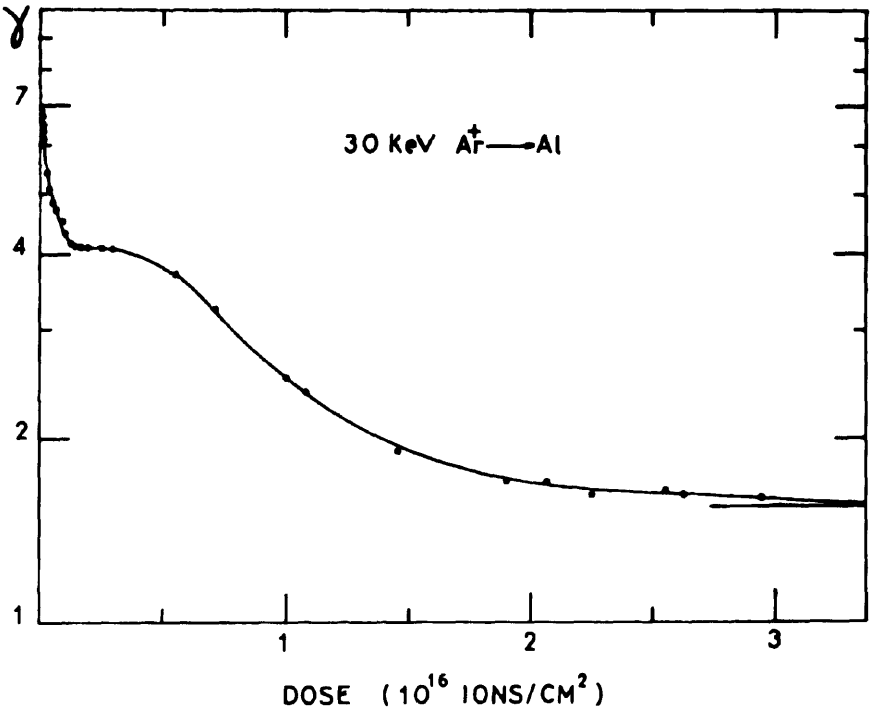

Fig. 3.8: Electron yields γ versus ion dose for 30 keV Ar^+ on an Al sample initially covered with air-formed oxide, measured by Baragiola et al. [55].

Fig. 3.8 shows similar result obtained by Baragiola et al. [55]. They used a 30 keV argon ion beam as a primary beam and ultra-high vacuum system (10^{-10} torr) to avoid oxidation by residual gas. The shape of the curve in Fig. 3.8 is very similar to the curves for 32x magnification in Fig. 3.5-7. Since surface oxidation due to adsorption of residual gas can be neglected in the condition used by Baragiola et al. because of UHV condition, it is clear that the change of the secondary yield with ion dose in Fig. 3.8 result from only sputtering effect. Accordingly, it seems reasonable to suppose that secondary yields in the curves of 32x magnification in Fig. 3.5-7 are hardly influenced by residual gases but are affected by sputtering. The important differences of experimental condition between the present work and Baragiola et al. are ion species, ion energy, and target environment (vacuum condition), because ion species and its energy determine sputtering yield that defined by the number of removed atoms per incident ion and target environment controls arrival rate of residual gas molecules at the target surface.

In order to investigate the sputtering effect on the secondary electron yield, additional experiments were performed using gold ions (Au^{2+}) as incident beams, since gold should have higher sputtering yield than silicon ion at the same energy because of its

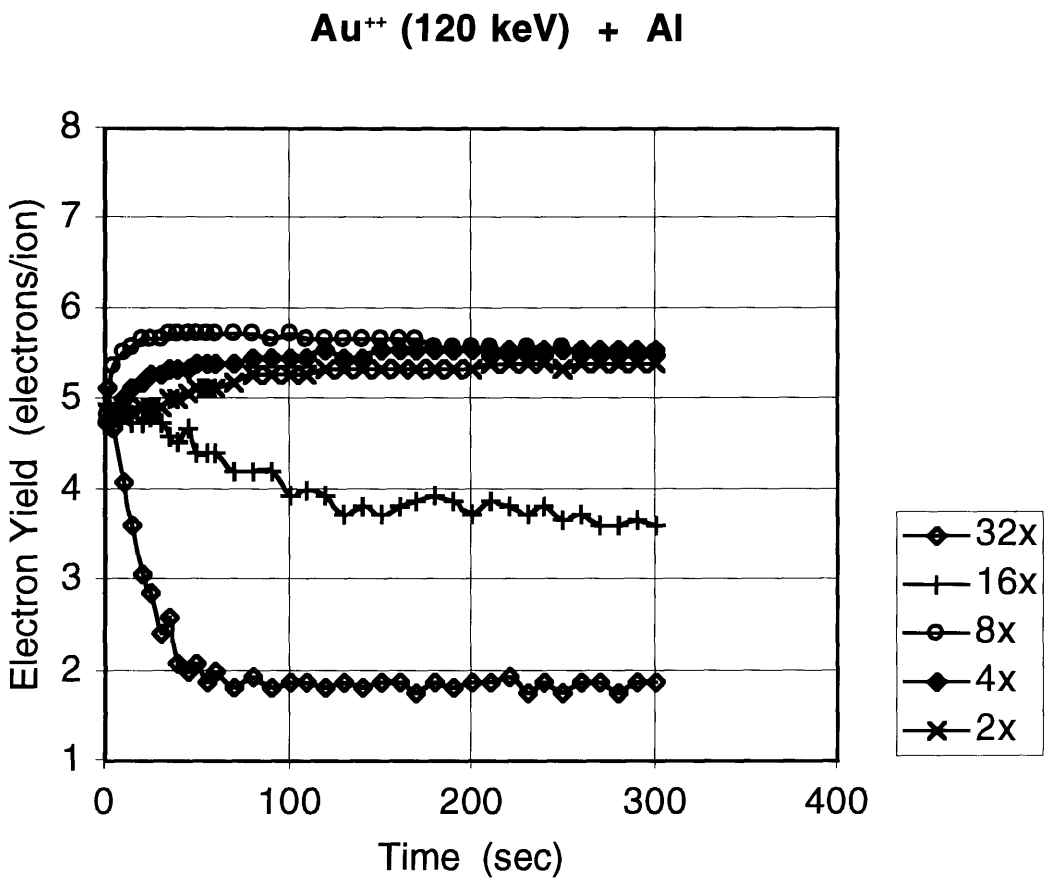

Fig. 3.9: Secondary electron yields from Al induced by 120 keV Au^{2+} as a function of irradiation time. Each line corresponds to a different scanning magnification (see Table 3.1).

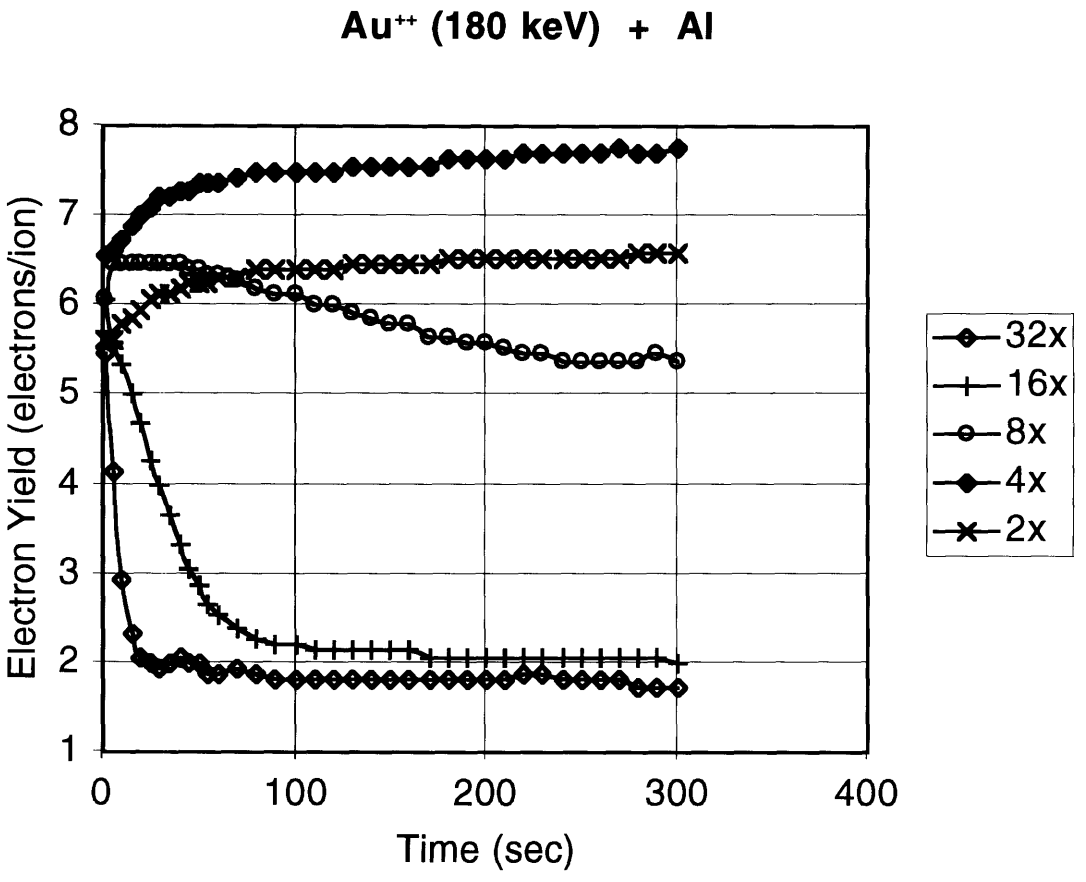

Fig. 3.10: Secondary electron yields from Al induced by 180 keV Au^{2+} as a function of irradiation time. Each line corresponds to a different scanning magnification (see Table 3.1).

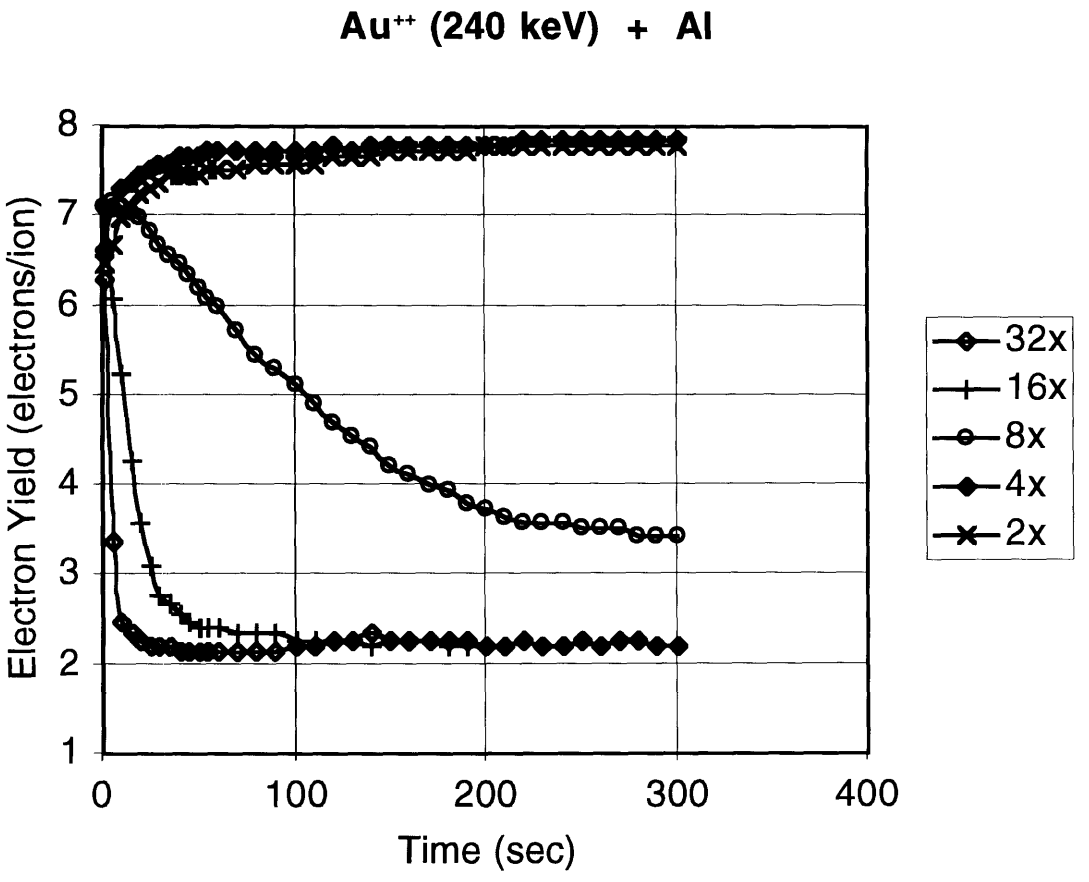

Fig. 3.11: Secondary electron yields from Al induced by 240 keV Au^{2+} as a function of irradiation time. Each line corresponds to a different scanning magnification (see Table 3.1).

heavier mass. The results are shown in Fig. 3.9, 3.10, and 3.11. In these measurements, the ion beam current was 30 pA compared to 40 pA for Si^{2+} beams. The data for Au ions indicate significantly higher sputtering yield despite having a lower average current density than Si^{2+} beams: secondary yields rapidly dropped for high magnification; curves for intermediate magnifications that show increases in the case of Si ion incidence show decreases with time. These results imply that the sputtering effect is one of the dominant processes to determine the tendency of the secondary yield curves for Al targets as well as for Si targets.

To discuss the difference between Si and Al targets, sputtering yield data for both materials may be required. However, such data for Si ion incidence are not available so that the data for Ar incidence will be used in this discussion. Experimental sputtering yield data by 5 keV Ar^+ for Al and Si targets are summarized in Table 3.2 along with those of oxides [56-58]. Since the surfaces of targets used in this work are covered by the native oxide, data for oxides will be meaningful for comparison between Si and Al targets. According to Table 3.2, sputtering yields for SiO_2 and Al_2O_3 are comparable. Consequently, removal rates of the surface atom for Si and Al targets may be the same order of magnitude, if one can assume that the dependence of sputtering yield on the target materials for Ar ions has the same tendency for Si ion incidence. Thus one may conclude that the observed difference in the secondary yields are due mainly to the difference of surface chemistry between Si and Al.

Referring to the Ellingham diagram the free energy of formation of Al_2O_3 is lower than that of SiO_2 so that aluminum is oxidized more easily than silicon. Hence the probability of oxidation, R_{ox}, for Al may be larger than R_{ox} for Si and the rate of oxidation of Al_2O_3 may be faster than that of SiO_2. This suggests that it will take a longer time to remove the surface oxide of aluminum than silicon because the rate of oxidation of Al_2O_3 is so fast that effective sputter removal rate decreases. This agrees with the observed results

Si [56]	**SiO_2** [57]	**Al** [58]	**Al_2O_3** [57]
1.2	**1.05**	**2.0**	**0.9**

Table 3.2: Experimental sputtering yield data by 5 keV Ar^+ for Si, Al, and their oxides in units of average number of atoms sputtered per incident ion.

that indicate a longer decay time required to reach the minimum of the secondary electron yields for Al targets than Si targets in high magnification curves. However, the increases of the yields for Al targets in intermediate magnification curves is not easy to explain. If oxide formation is so fast that the thickness of oxide layer increases during ion irradiation, the lowest magnification would have the fastest growth rate because of the lowest sputtering rate. And if secondary electron yield is strongly related to the oxide thickness, then thicker oxide would result in higher electron yield. This assumption may be true when the thickness is less than electron escape depth, since escape depth for oxides (30-300 Å) is nearly one order of magnitude larger than that for metals (5-20 Å) and is thicker than the thickness of native oxide (5-50 Å) [51] [52]. Hence the lowest magnification curves might show the largest increases. This, however, disagrees with observed results such that only intermediate magnification curves show increases. Therefore, this observed phenomena cannot be explained only by surface chemistry. It must involve ion bombardment effects, such as those observed in plasma-enhanced oxidation process.

3.3 Results on PMMA Target

Si ion induced secondary electron yields of PMMA for various ion energies were also measured as a function of irradiation time using the same method as previously described. Fig. 3.12-14 show the results.

These curves show considerably different characteristics from those shown previously; the yields in higher magnification curves increase with time. There is no readily available data to evaluate sputtering effect on polymer. Data about secondary electron emission from polymers is also lacking because polymer is insulator so that it is extremely difficult to measure the true secondary yield due to the sample charging-up. In this work, however, effective secondary electron yields, which are related to an amount of electrons that can be detected by electron detectors, are the objective of measurements for practical purpose. Hence, even if the data is influenced by charge-up effect, it has great relevance here. The charge-up effect may reduce secondary electron yield because positive ion bombardment results in positively charged surface condition and suppresses the electron emission from the surface. The higher the current density used, the more severe the charging. This suggests that secondary yield for high magnification may show lower value. On the contrary, the observed yield increases with ion current density. This may be due to some other ion bombardment effect such as ion induced conduction. However, there is too little information to evaluate this phenomena.

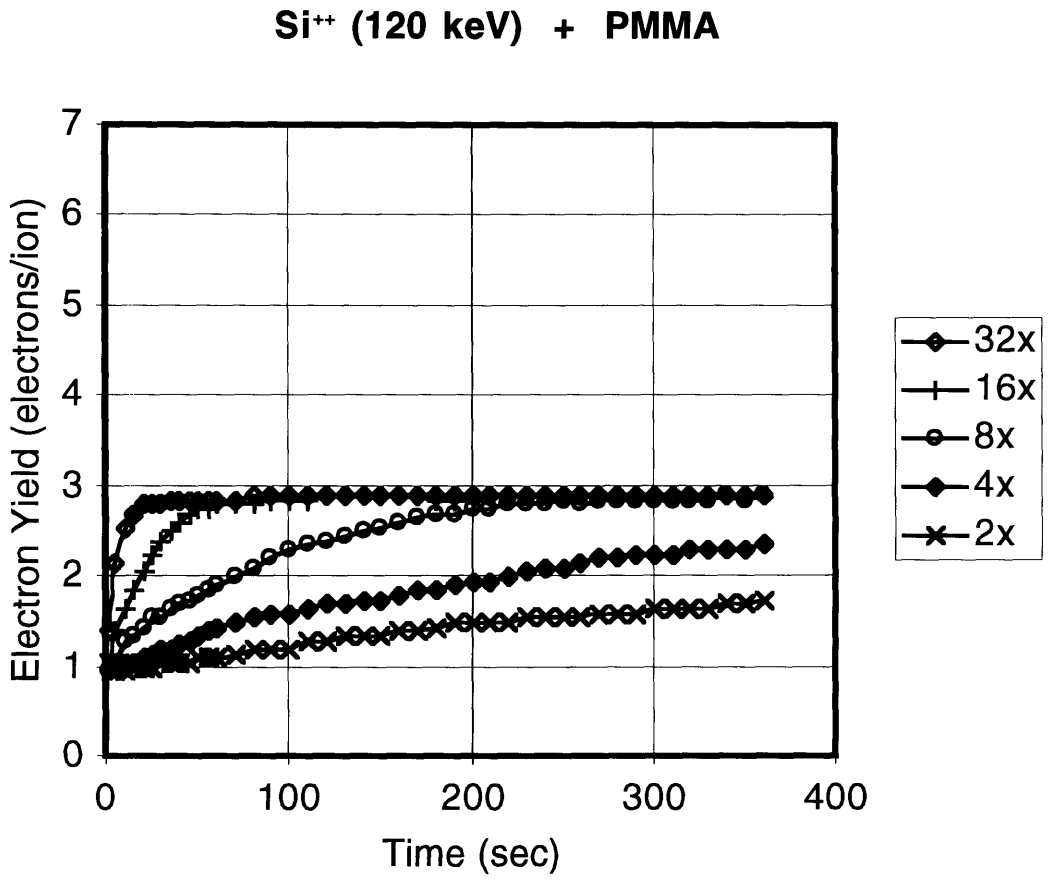

Fig. 3.12: Secondary electron yields from PMMA induced by 120 keV Si^{2+} as a function of irradiation time. Each line corresponds to a different scanning magnification (see Table 3.1).

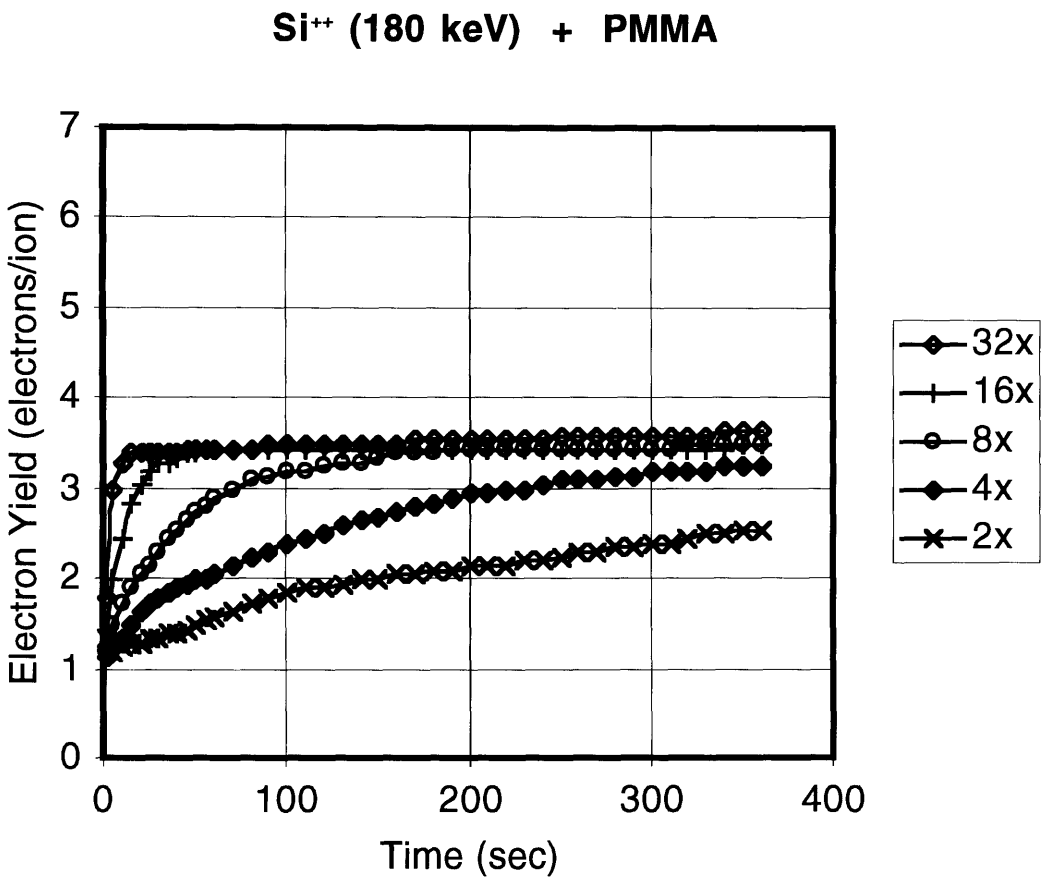

Fig. 3.13: Secondary electron yields from PMMA induced by 180 keV Si^{2+} as a function of irradiation time. Each line corresponds to a different scanning magnification (see Table 3.1).

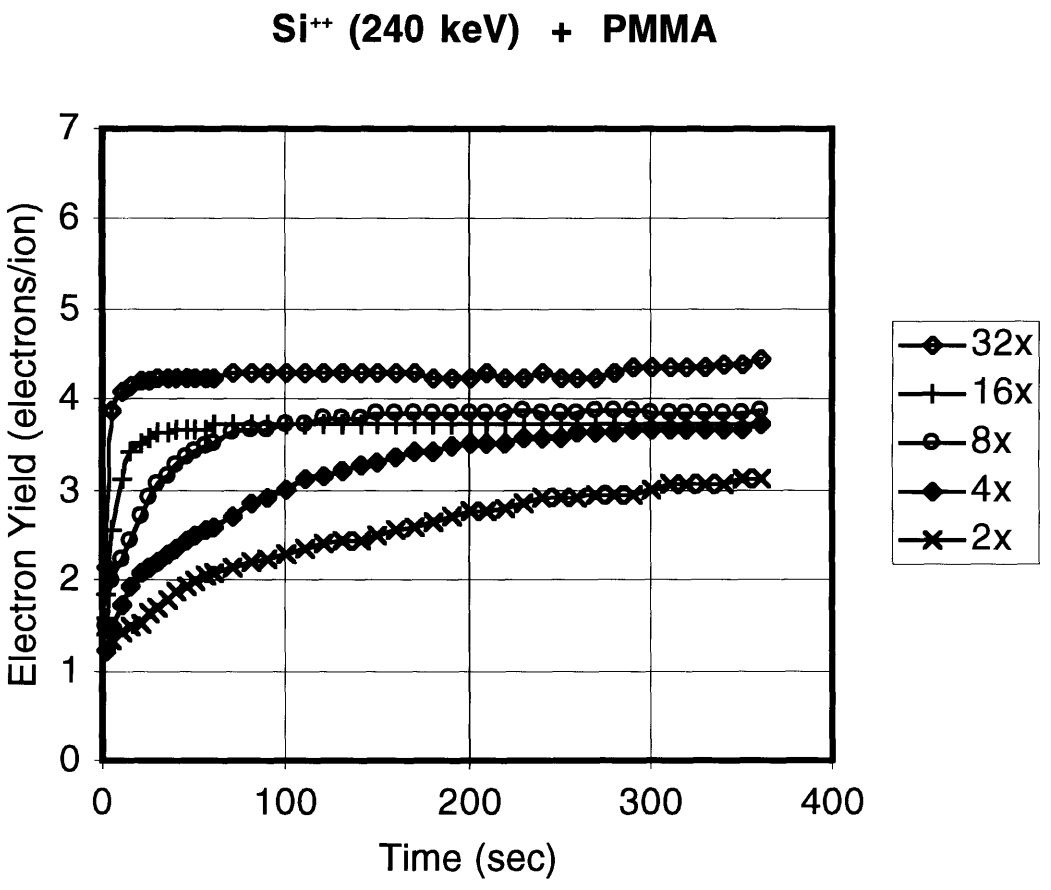

Fig. 3.14: Secondary electron yields from PMMA induced by 240 keV Si^{2+} as a function of irradiation time. Each line corresponds to a different scanning magnification (see Table 3.1).

For practical purpose in applying spatial-phase-locking to FIB lithography, the secondary electron yield at very short intervals is the most important parameter, because ion beams cannot be scanned over the sample surface for long periods of time to without undesirable exposure of resist. The measured yields at time≈0 show reasonably consistent energy dependence (the yields increase with the ion energy). Secondary electron yield measurements of PMMA allows the evaluation of possible contrast that will be obtained from a fiducial grid.

3.4 Feasibility of Detection of a Fiducial Grid

When one applies the spatial-phase-locking method to particle-beam lithography, the signal-to-noise ratio of the fiducial-grid signal is extremely important since it determines the ability to use the signal as a reference of the beam position. The detectability will be evaluated by the intensity of the secondary signal per incident particle which strongly depends on the secondary yield, while the reliability will be evaluated by the contrast of the signal which relates to the ratio of the secondary yields between the materials that constitute the fiducial grid. H. I. Smith et al. have analyzed the feasibility of detecting the fiducial grid when an electron beam is used as a incident beam [47]. In this section, the feasibility of detecting the fiducial grid will be evaluated, when an FIB is used as an incident beam, by following the approach given by them.

Fig. 3.15 illustrates a basic idea of the analysis. When an incident beam is line-scanned across the unit cell of the global-fiducial grid, the intensity of the secondary signal will change with time as shown in Fig. 3.15(b). Here, n_s gives a secondary signal intensity per pixel time interval t_p. n_{sw} and n_{sb} are the average signal intensities (per t_p) of white and black level respectively in a binary image obtained experimentally. n_i is the mean number of ions impinging on the substrate during t_p.

From Fig. 3.15(b), $(\delta_A + \delta_B)\, n_i = n_{sw}$ and $\delta_B\, n_i = n_{sb}$. In the case of ion incidence, the background signal due to backscattering electrons and/or stray electrons is negligible, in contrast to the case of electron incidence. Therefore, the intensity of the signal consists of only "true" secondaries while in the case of electron incidence the signal includes true secondaries and background. Hence, one can assume that $n_{sw} = k\, \gamma_w\, n_i$ and $n_{sb} = k\, \gamma_b\, n_i$, where k is the collection efficiency of the secondary detection system, γ_w and γ_b are the secondary yields for the materials used to make the fiducial grid. The two levels have to be

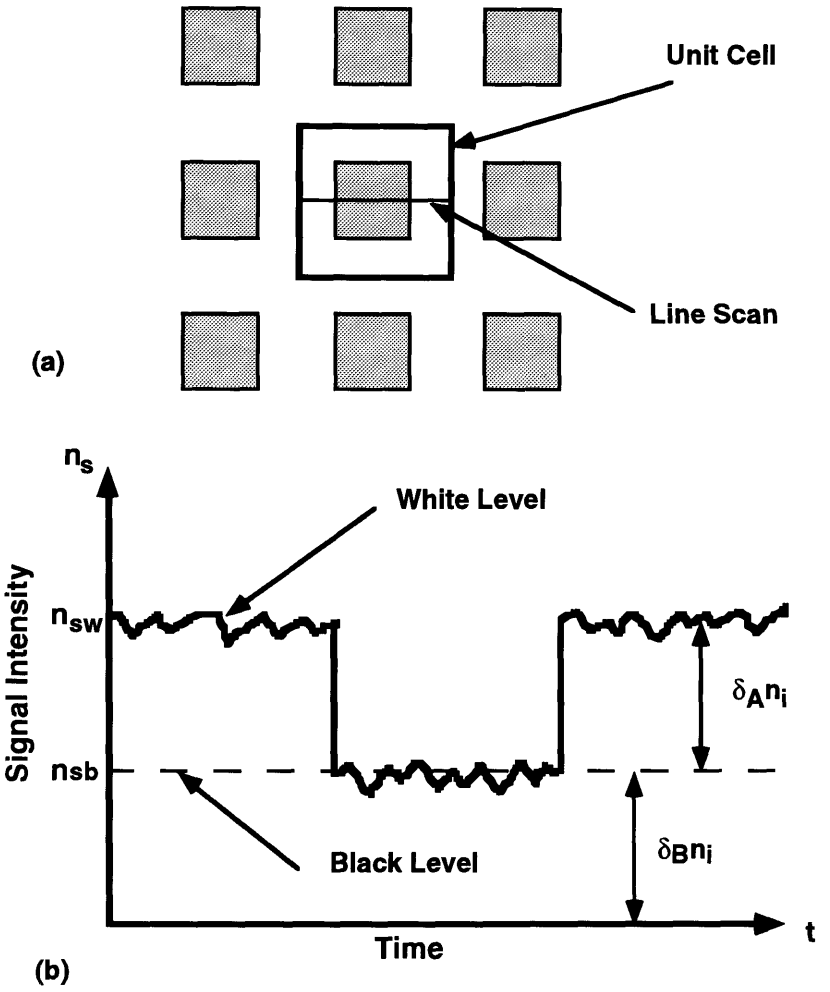

Fig. 3.15: (a) Sketch of one unit cell of the global-fiducial grid. (b) Depiction of the secondary signal intensity n_s, per pixel time interval t_p, for a line scan across the middle of the unit cell. A binary image (i.e., black islands on a white background) is to be formed [47].

separated well enough to distinguish between them. Let the levels be separated by m standard deviations: $\delta_A n_i = m\,\sigma = m\,\sqrt{n_{sb}}$. Therefore,

$$n_i = \frac{m^2 \delta_B}{\delta_A^2} = \frac{m^2 \gamma_b}{k(\gamma_w - \gamma_b)^2}. \qquad (3.3)$$

Thus, for a given confidence level m and a given collection efficiency k one can calculate how many ions are required per t_p, using the measured secondary yields.

Fig. 3.16 shows the initial secondary yields (the values at the beginning of ion irradiation) for various ion-target combinations measured in this work. When a 240 keV Si^{2+} beam is used as an incident beam and Al and PMMA are the materials used in the

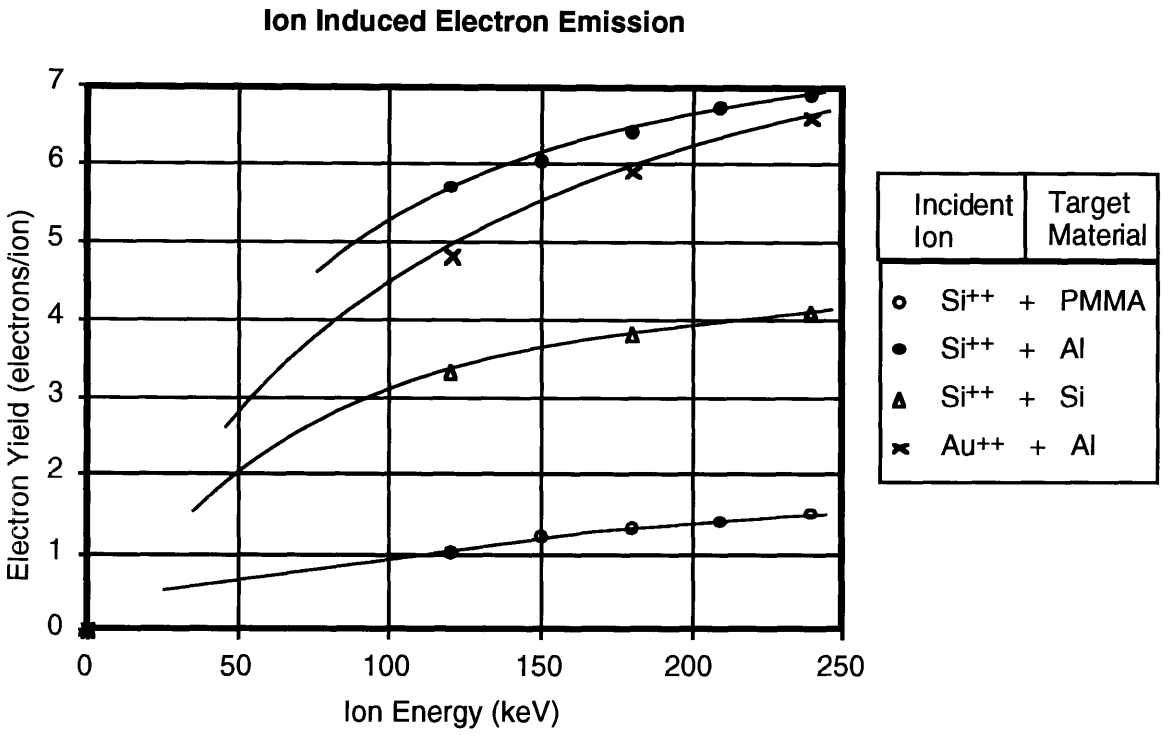

Fig. 3.16: Initial secondary electron yields versus ion energy for various ion-target combinations measured in this work.

fiducial grid, $\gamma_w \approx 6.9$ and $\gamma_b \approx 1.5$. To view a portion of the global fiducial grid an areal dose given by:

$$D = n_i(L^2 / A) \tag{3.4}$$

is required, where L is the number of line scans (i.e., L^2 is the total number of pixels) and A is the area being viewed. Assuming a collection efficiency of 10% ($k = 0.1$), $m = 3$, $L = 100$, and $A = 10 \times 10$ μm^2, the required dose is

$$D = 4.6 \times 10^{10} \text{ ions cm}^{-2}. \tag{3.5}$$

This value is two order of magnitude smaller than the dose required to expose a resist such as PMMA (typically ~10^{13} ions cm^{-2} [8], see Fig. 1.15). In this case, the redundancy factor defined by the number of unit cells contained in the scan field is 2.5×10^3 for a 0.2-μm period grid. Hence, the fiducial grid will readily be detected using the signal from FIB induced secondary electrons without disturbing the writing process.

3.5 Evaluation of Sputtering and Oxidation Effects on Secondary Electron Emission

In order to estimate the effects of oxidation by residual gas and sputtering on the secondary electron yield, computation using a simple model will be presented in this section.

As described in previous sections, FIB induced secondary electron emission depends strongly on the surface condition of the target. During ion irradiation the surface condition is continuously changing by the influence of oxidation and sputtering. For example, the oxidation process transforms Si atom on the surface into SiO_2 by adding oxygen, while the sputtering process removes the components of the surface (Si and/or SiO_2) and uncovers the underlying Si atoms; one process is additive, the other is subtractive. Therefore, the competition of these two processes governs the rate of change of the surface condition. Here, let the proportion of surface atoms that are oxide be x_o and that of unoxidized atoms (pure, elemental atom) be x_m. Thus, $x_o + x_m = 1$, assuming that there is no other atom added (e.g., nitrogen). As described before, the oxidation rate may be expressed by $(J_{gas}\, Rox)$, and the sputtering rate may be expressed by $(J_{ion}\, S)$. When a Si atom is removed by sputtering, another, underlying Si atom is revealed at the surface. This results in no change of the surface composition so that only the sputtering yield for oxide, S_o, needs to be taken into account. The rate of change of each component at the surface may be given by the following equations:

for oxide:
$$\frac{dx_o}{dt} = \frac{J_{gas}R_{ox}}{\Omega} x_m - \frac{J_{ion}S_o}{\Omega} x_o, \tag{3.6}$$

and for pure element:
$$\frac{dx_m}{dt} = \frac{J_{ion}S_o}{\Omega} x_o - \frac{J_{gas}R_{ox}}{\Omega} x_m, \tag{3.7}$$

where Ω is the number of atom per unit area at the surface. In these equations, constant surface atomic density is assumed. The initial condition will be given by $x_o(0) = 1$, and $x_m(0) = 0$, because the surface is covered by native oxide. The solutions of these equations are:

$$x_o(t) = \frac{J_{gas}R_{ox}}{J_{gas}R_{ox} + J_{ion}S_o} + \frac{J_{ion}S_o}{J_{gas}R_{ox} + J_{ion}S_o} \exp(-\frac{J_{gas}R_{ox} + J_{ion}S_o}{\Omega} t), \tag{3.8}$$

$$x_m(t) = 1 - x_o(t). \tag{3.9}$$

Assuming that the secondary electron yield depends only on the surface atom composition (no effect by underlying atoms), the total secondary electron yield γ may be expressed as:

$$\gamma = \gamma_o x_o + \gamma_m x_m, \tag{3.10}$$

where γ_o and γ_m are the secondary yields for oxide and pure element, respectively. If one can obtain these parameters, the curves of the secondary yield versus the ion irradiation time may be reproduced using these equations.

From (3.8) and (3.10) it is apparent that the secondary yield by this model decreases monotonically with time because of the exponential term. This cannot explain, however, the observed tendency of some of the secondary electron yields for Al targets which increase with time. Other effects must be incorporated into the model to explain increasing secondary electron yield. These effects may include the influence of underlying atoms, the difference in electron escape depth of oxides and pure elements, diffusion of gas molecules through the surface, and ion induced effects such as ion enhanced oxidation, ion enhanced diffusion.

A result of the computation using this model for 240 keV Si^{2+} on Si target is shown in Fig. 3.17. The values used in this calculation are as follows:

- $J_{ion} = 7.1 \times 10^{14}$ ions/cm^2 sec, for 32x. This corresponds to a beam current of 40 pA scanning over a field of 4.2×4.2 μm^2. For the other magnifications J_{ion} is inversely proportional to the scanning area.
- $J_{gas} = 9.6 \times 10^{13}$ molecules/cm^2 sec, using $p = 2 \times 10^{-7}$ torr, M = 18 (H_2O), T = 297K in eq.(3.2).
- $\gamma_o = 4.2$, $\gamma_m = 2.5$, from Fig. 3.3 (γ_o = initial value at $t = 0$, γ_m = final value for 32x curve)
- $S_o = 0.2$, from the result of TRIM simulation for SiO_2 bulk target.
- $R_{ox} = 0.04$. R_{ox} was used as a fitting parameter. This value means that 4% of molecules arriving at the target surface contributes to the oxidation process.
- $\Omega = 6.8 \times 10^{14}$ atoms/cm^2, for (100) Si.

This calculated result shows qualitatively good agreement with the observed result of Fig. 3.3, especially for high magnification curves. Fig. 3.18 shows the result of this calculation for 32x and 16x magnifications along with the measured data.

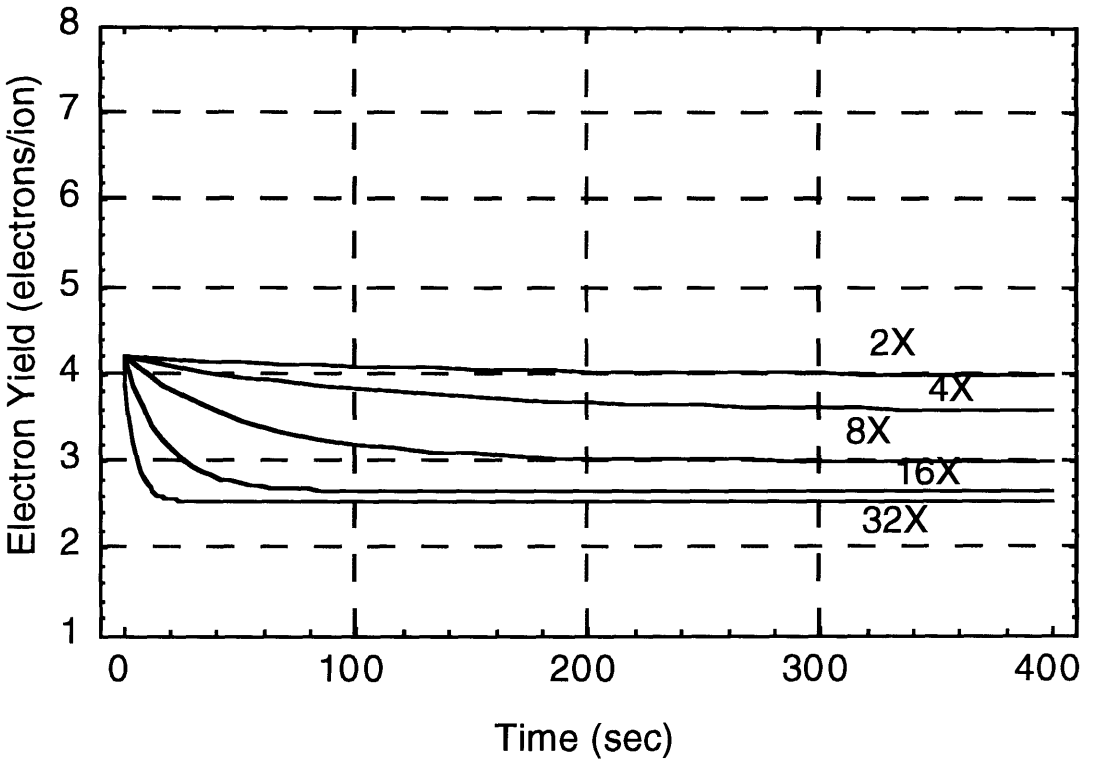

Fig. 3.17: Calculated secondary electron yields versus ion irradiation time for 240 keV Si^{2+} on Si target.

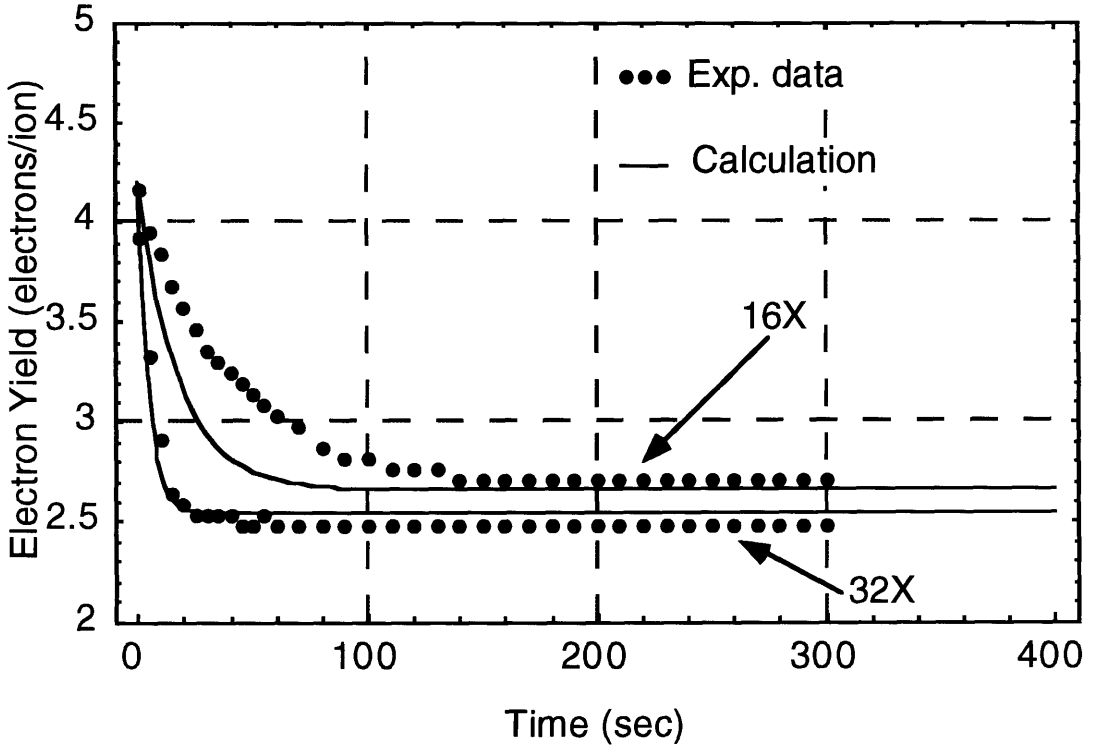

Fig. 3.18: Comparison of calculated electron yield and measured data for 240 keV Si^{2+} on Si target for magnifications of 16x and 32x.

4. Summary

Yields of FIB induced secondary electron from Si, Al, and PMMA targets have been measured to investigate the feasibility of spatial-phase-locked FIB lithography. The results indicate that Al has very high secondary electron yield ranging from 5.7 to 6.9 electrons per ion for 120-240 keV Si^{2+} incidence, and PMMA has very low secondary yield ranging from 1.0 to 1.5 electrons per ion for the same ion irradiation conditions. These results lead to the conclusion that a fiducial grid fabricated on a substrate will be imaged with sufficient contrast by means of detecting FIB induced secondary electrons. Furthermore, the image obtained by FIB will have a much better signal-to-noise ratio than the image obtained by electron beams because of the fact that ion bombardment produces almost no backscattering electron. The required ion dose to detect the fiducial-grid signal with appropriate contrast have been calculated. The calculated value is much lower than the ion dose required to expose resist. Thus, it is possible to detect the grid signal without disturbing the writing. It seems reasonable to conclude, from what has been discussed above, that spatial-phase-locked focused-ion-beam lithography will be a promising tool to fabricate nanometer range resolution with high accuracy and precision.

In this work, secondary electron yields as a function of ion irradiation time have also been measured. When plotting the results of the secondary yields versus time, considerable differences in the tendency of the curves are observed depending on the target materials. An explanation of the observed results was attempted in terms of two competing processes: sputtering by incident ions and oxidation by residual gases. For Si target, the results can be illustrated quite naturally as due to the two processes. That is, removal of native oxide by sputtering results in a decrease of secondary yield with time for high current density, and for low current density the surface remains oxidized due to reaction of residual gases and the surface atoms and thus the secondary yield shows little change with time. For Al target, however, this model cannot explain all of the observed results. In some cases, an increase of the secondary yields with time has been observed. These results will require some further explanations in terms of the characteristics of aluminum and ion irradiation induced chemical effects.

References

[1] L. F. Thompson, C. G. Willson, and M. J. Boeden, *Introduction to Microlithography* (American Chemical Society, Washington, D. C., 1983)

[2] S. Wolf and R. N. Tauber, *Silicon Processing for the VLSI Era* (Lattice Press, Sunset Beach, 1986)

[3] Semiconductor Industry Association, 1992

[4] D. Kyser and N. S. Viswanathan, *J. Vac. Sci. Technol.*, **12,** 1305 (1975)

[5] A. M. Hawryluk, R. J. Hawryluk, and H. I. Smith, *J. Appl. Phys.* **45**, 2551 (1974)

[6] H. I. Smith, *Submicron- and Nanometer-Structures Technology,* (NanoStructure Press, Sudbury, 1994)

[7] W. Chu, A. Yen, K. Ismail, M. I. Shepard, H. J. Lezec, C. R. Musil, J. Melngailis, Y. C. Ku, J. M. Carter, and H. I. Smith, *J. Vac. Sci. Technol. B* **7**, 1583 (1989)

[8] S. Matsui, Y. Kojima, Y. Ochiai, and T. Honda, *J. Vac. Technol. B* **9**, 2622 (1991)

[9] R. L. Kubena, J. W. Ward, F. P. Stratton, R. J. Joyce, and G. M. Atkinson, *J. Vac. Technol. B* **9**, 3079 (1991)

[10] J. Melngailis, *Nucl. Instrum. Methods B* **80/81**, 1271 (1993)

[11] R. Clampitt, R. Aitken, and D. K. Jefferies, *J. Vac. Technol.* **12**, 1208 (1975)

[12] V. E. Krohn and G. R. Ringo, *Appl. Phys. Lett.* **27**, 479 (1975)

[13] R. L. Seliger, J. W. Ward, V. Wang, and R. L. Kubena, *Appl. Phys. Lett.* **34**, 310 (1979)

[14] A. Wagner, *Nucl. Instrum. Methods* **218**, 355 (1983)

[15] A. Wagner and T. M. Hall, *J. Vac. Sci. Technol.* **16**, 1871 (1979)

[16] W. L. Brown and A. Wagner, in *Proc. ISIAT '83 & IPAT '83, Kyoto,* p.1738A (Institute of Electrical Engineering of Japan, Japan, 1983)

[17] L. W. Swanson, *Nucl. Instrum. Methods* **218**, 347 (1983)

[18] P. D. Prewett, G. L. R. Mair, and S. P. Thompson, *J. Phys. D* **15**, 1339 (1982)

[19] J. W. Ward and R. L. Seliger, *J. Vac. Technol.* **19**, 1082 (1981)

[20] M. Komuro, T. Kanayama, H. Hiroshima, and H. Tanoue, *Appl. Phys. Lett.* **42**, 908 (1983)

[21] J. Orloff, *Rev. Sci. Instrum.* **64**, 1105 (1993)

[22] A. E. Bell, K. Rao, G. A. Schwind, and L. W. Swanson, *J. Vac. Technol.B* **6**, 1927 (1988)

[23] G. L. R. Mair, *J. Phys. D* **20**, 1657 (1987)

[24] M. Komuro and T. Kato, *J. Physique* **48**, C6, 141 (1987)

[25] T. Ishitani, Y. Kawanami, T. Ohnishi, and K. Umemura, *Appl. Phys. A* **44**, 233 (1987)

[26] A. Yasaka, T. Yamaoka, T. Kaito, and T. Adachi, *J. Vac. Sci. Technol. B* **9**, 2642 (1991)

[27] E. Miyauchi, H. Arimoto, H. Hashimoto, T. Furuya, and T. Utsumi, *Jpn. J. Appl. Phys.* **22**, L287 (1983)

[28] L. R. Harriott, in *Beam Processing Technologies*, VLSI Electronics Microstructure Science vol. 21, ed. N. G. Einspruch, S. S. Cohen, and R. J. Singh, p.157 (Academic Press, San Diego, 1989)

[29] M. Sato and J. Orloff, *J. Vac. Technol.B* **9**, 2602 (1991)

[30] P. Marriott, *Appl. Phys. A* **44**, 329 (1987)

[31] K. D. Cummings, L. R. Harriott, G. C. Chi, and F. W. Ostermayer, Jr., *Proc. SPIE* **632**, 93 (1986)

[32] J. F. Ziegler, J. P. Biersack, and U. Littmark, *The Stopping and Range of Ions in Solids* vol. 1, ed. J. F. Ziegler (Pergamon Press, New York, 1985)

[33] J. Melngailis, *J. Vac. Technol. B* **5**, 1469 (1987)

[34] P. D. Prewett and G. L. R. Mair, *Focused Ion Beams from Liquid Metal Ion Sources* (Research Studies Press, Somerset, England, 1991)

[35] K. Gamo, *Semicond. Sci. Technol.* **8**, 1118 (1993)

[36] D. K. Atwood, G. J. Fisanick, W. A. Johnson, and A. Wagner, *Proc. SPIE* **471**, 127 (1984)

[37] M. Yamamoto, M. Sato, H. Kyogoku, K. Aita, Y. Nakagawa, A. Yasaka, R. Takasawa, and O. Hattori, *Proc. SPIE* **632**, 97 (1986)

[38] J. Melngailis, C. R. Minsoll, E. H. Stevens, M. Utlaut, E. M. Kellog, R. T. Post, M. W. Geis, and R. W. Mountain, *J. Vac. Sci. Technol. B* **4**, 176 (1988)

[39] Y. Mashiko, H. Morimoto, H. Koyama, S. Kawazu, T. Kaito, and T. Adachi, in *Proc. of the 25th International Reliability Physics Symp.,* p.111 (IEEE, New York, 1987)

[40] A. Wagner and J. P. Levin, *Nucl. Instrum. Methods B* **37/38**, 224 (1989)

[41] J. Schou, *Scanning Microsc.* **2**, 607 (1988)

[42] D. Hasselkamp, in *Particle Induced Electron Emission II, Springer Tracts in Mod. Phys.* vol. 123, ed. G. Höhler, p.1 (Springer-Verlag, Berlin, 1992)

[43] K. Nikawa, N. Nasu, M. Murase, T. Kaito, T. Adachi, and S. Inoue, in *Proc. of the 27th International Reliability Physics Symp.,* p.43 (IEEE, New York, 1989)

[44] Seiko Instruments Inc., Japan, Private Communication

[45] J. A. Randall, M. A. Reed, R. J. Matyi, T. M. Moore, R. J. Aggawal, and A. E. Westel, *Proc. SPIE* **945**, 137 (1988)

[46] S. Matsui, Y. Kojima, and Y. Ochiai, *Appl. Phys. Lett.* **53**, 868 (1988)

[47] H. I. Smith, S. D. Hector, M. L. Schattenburg, and E. H. Anderson, *J. Vac. Technol. B* **9**, 2992 (1991)

[48] J. Ferrera, V. V. Wong, S. Rishton, V. Boegli, E. H. Anderson, D. P. Kern, and H. I. Smith, *J. Vac. Technol. B* **11**, 2342 (1993)

[49] J. Ferrera, *Highly Coherent Gratings for Optoelectronics: An Application of Spatial-Phase-Locked Electron Beam Lithography*, SM Thesis, MIT, 1994

[50] V. Wang, J. W. Ward, and R. L. Seliger, *J. Vac. Technol.* **19**, 1158 (1981)

[51] C. J. Tung, J. C. Ashley, R. D. Birkhoff, R. H. Ritchie, L. C. Emerson, and V. E. Anderson, *Phys. Rev. B* **16**, 3049 (1977)

[52] J. C. Ashley, C. J. Tung, and R. H. Ritchie, *Surf. Sci.* **81**, 409 (1979)

[53] A. J. Dekker, *Solid State Physics* (Prentice-Hall, Englewood Cliff, 1957)

[54] S. M. Sze, ed. *VLSI Technology* (McGraw-Hill, New York, 1985)

[55] R. A. Baragiola, E. V. Alonso, J. Ferron, and A. Oliva-Florio, *Surf. Sci.* **90**, 240 (1979)

[56] A. Southern, W. R. Willis, and M. T. Robinson, *J. Appl. Phys.* **34**, 153 (1963)

[57] H. Bach, *Nucl. Instrum. Methods*, **83**, 4 (1970)

[58] O. C. Yonts, C. E. Normand, and D. E. Harrison, *J. Appl. Phys.* **31**, 447 (1960)